

ANALYTICAL AND NUMERICAL STUDIES ON MISMATCH STRAIN
RELATED PROBLEMS

BY

NAN LI

THESIS

Submitted in partial fulfillment of the requirements
for the degree of Master of Science in Mechanical Engineering
in Graduate College of the
University of Illinois at Urbana-Champaign, 2016

Urbana, Illinois

Adviser:

Professor K. Jimmy Hsia

Abstract

This thesis presents the analytical, numerical, and experimental study on mismatch strain related problems. Three problems are analyzed: self-assembling of polymer thin film, failure of nanotube and nanorod silicon anodes in lithium batteries and modified failure criterion for earthquake distribution along the earth depth.

The first chapter discusses analytical and experimental results of self-assembling of thin films made from Polydimethylsiloxane (PDMS)/SU-8 mixture. Material properties can be changed by ultraviolet (UV) light exposure. Gradients of material properties, swelling ratio and young's modulus, leads to self-assembling in Toluene solution. An analytical model based on beam theory and principle of minimum potential energy was used to predict the folding directions. In order to have a better control of the folding mechanism, ABAQUS models were developed and experiments were conducted with different UV exposure patterns to calibrate both diameters of patterned polymer rolls and angles of partially patterned polymer after assembling. With results from calibration, more complex structures, such as one-degree-of-freedom origami, were designed and fabricated.

The second chapter gives failure analysis of nanotube and nanorod silicon anodes in lithium batteries. Silicon is a promising material for lithium batteries with greater energy density. However, silicon has up to 400% volume dilation after lithiation. Large deformation causes mismatch strain and stress between lithiated silicon and non-lithiated silicon and leads to functional failure eventually, especially under repeated lithiation-delithiation cycles. New structures have been proposed by different researchers to avoid functional failure of silicon anodes. A nanotube structure was proposed and compared with previous nanorod structure. ABAQUS models and analytical models were developed to study stress and strain evolution during lithiation process in both nanorod and nanotube structures. Low- cycle fatigue theory was used to explain failure of both structures.

In the last chapter, a modified Mohr-Coulomb failure criterion is developed to explain earthquake frequency distribution along the earth depth. It was found that earthquake happened more frequently around 20 and 600 kilometers. To explain the distribution, a new model based on

mismatch strain between crust and mantle was proposed by geologists. In their model, crust and mantle had different volume reduction at different depth of the earth. Stress in crust was caused by the mismatch between crust and mantle and varied along the depth. A failure criterion was required to determine if the fracture happened. A nonlinear Mohr- Coulomb failure criterion was developed. The criterion states that ultimate shear stress of rocks will be increased by raising the hydrostatics pressure. It is promising to explain earthquake distribution along the earth depth with stress distribution data from ABAQUS model.

Acknowledgment

I want to express my sincere gratitude to Professor K. Jimmy Hsia for his continuous support and guidance throughout my research. His scientific spirit inspired me a lot. I will be grateful for that forever. I also want to thank my colleagues: Daniel Perlitz, Arif Md Abdullah, Gubeum Kwon (Gavin), Yutao Han (Dylan), Christopher M. Daly and Jinyun Liu. They kindly offered their help when I had problems with my numerical model development and experimental setup.

Table of Content

List of Figures.....	vii
List of Tables	xi
Chapter 1 : Self-Assembly of PDMS/SU-8 Films	1
1.1 Introduction	1
1.2 Analytical model for predicting folding directions	2
1.2.1 Simplified geometry	2
1.2.2 Analytical methods.....	4
1.2.3 Results and discussion	10
1.3 Experimental calibration of radius of curvature	13
1.3.1 Sample fabrication	13
1.3.2 Experimental setup and image processing methods	16
1.3.3 Results and discussion	18
1.4 FEA prediction and experimental calibration of folding angle	19
1.4.1 Preliminary FEA implement	20
1.4.2 Sample preparation, experimental setup and image processing	23
1.4.3 Results and discussion	25
1.5 Origami with Polymer film.....	27
1.5.1 Surface angle relationship	28
1.5.2 Exposure pattern and photomask design	31
1.5.3 Results and discussion	33
1.6 Future work	35
Chapter 2 : Failure of Silicon Anodes in Lithium Battery	37
2.1 Introduction	37
2.2 FEA model for stress and strain evolution	38
2.2.1 FEA implement	38
2.2.2 Results and discussion	40
2.3 Analytical model for stress distribution	42
2.4 Future work	44
Chapter 3 : Modified Mohr-Coulomb Criterion	46
3.1 Introduction	46
3.2 Failure criteria, envelopes and surfaces.....	47

3.2.1 Tresca criterion	47
3.2.2 Von Mises criterion	48
3.2.3 Mohr-Coulomb criterion	50
3.3 Experimental results from literature.....	51
3.4 Nonlinear Mohr-Coulomb failure envelope for earthquake frequency	53
3.5 Future work	58
References	59

List of Figures

Figure 1.1: Fluorescence images of polymer films and simplified geometry: a) cross-section of 600-micron spacing samples; b) top-view of 100-micron spacing samples (with a different filter); c) simplified cross-section of polymer.....	3
Figure 1.2: Folding modes: a) folding mode 1: top layer wraps up the bottom in parallel direction; b) folding mode 2: bottom layer wraps up the top in normal direction. [15]	4
Figure 1.3: Bilayer-beam structure before and after bending	4
Figure 1.4: Deflection and strain energy comparison between numerical solution, solution for generalized plane strain condition and Timoshenko's solution.....	9
Figure 1.5: Scatter plot and boundaries of two folding modes: a) with respect to swelling ratio with fixed $Exn = 6.66$ and $Epn = 5.01$ b) with respect to Young's modulus with fixed $\alpha xn = 0.323$ and $\alpha pn = 0.632$	11
Figure 1.6: Changes of boundaries between two folding modes with different Exn and Epn : (a) increasing Exn from 1 to 10 with $Epn = 5.01$; (b) increasing Epn from 1 to 10 with $Exn = 6.66$	12
Figure 1.7: Changes of boundaries between two folding modes with different αxn and αpn : (a) increasing αxn from 0 to 1 with $\alpha pn = 0.632$; (b) increasing αpn from 0 to 1 with $\alpha xn = 0.323$	13
Figure 1.8: Mixture of PDMS/SU-8 at different steps: (a) mixture before stirring; transparent liquid is the PDMS; yellow liquid is SU-8; (b) mixture after stirring; mixture turns to be milk white; bubbles present on the surface; (c) mixture after degassing; bubbles are removed by vacuum. Mixture is in a disposable plastic petri dish	14
Figure 1.9: Glass slides at different process: (a) apply Kapton tape on the glass slide; back of a razor blade pushes against glass slides to remove bubbles; (b) mixture distributed on glass slides; center and two ends of glass slides have mixture; (c) glass slide with thin film after spincoating	14
Figure 1.10: Glass petri dish: (a) empty dish with aluminum cover on the left and paper towel inside; (b) dish with 5 samples inside after curing; the picture was taken in cleanroom	15
Figure 1.11: Sample cutting fixture: (a) front view of the fixture; (b) bottom view of the fixture	16
Figure 1.12: Experiment setup for radius of curvature calibration	16
Figure 1.13: Final profiles of samples with different XL spacing in the toluene	17

Figure 1.14: Image processing procedures: (a) vertical line for pixel and millimeter conversion; (b) diameter calibration by circular fitting.....	17
Figure 1.15: Spacing and diameter scattering with 30%wt SU-8: (a) with Aluminum cover during curing process (b) without Aluminum cover during curing process.....	18
Figure 1.16: Conceptual design and expected folding shape.....	19
Figure 1.17: Material sections and boundary conditions of quart of the sample.....	21
Figure 1.18: Different mesh on different regions on the sample	22
Figure 1.19: Final profiles of polymer samples with different pattern length, spacing and thickness ratio from top to bottom.....	23
Figure 1.20: Final angles of different patterns.....	24
Figure 1.21: Angle measurement in ImageJ	24
Figure 1.22: Final angles in degrees as a function of pattern length: (a) for 100-micron-spacing; (b) for 200-micron-spacing;.....	25
Figure 1.23: Idealized geometry of final angle	25
Figure 1.24: Comparison between numerical and experimental results: (a) for 100-micron-spacing; (b) for 200-micron-spacing.....	26
Figure 1.25: One-degree-of- freedom origami structure: (a) crease pattern; (b) (c) (d) structures determined by different surface angles	28
Figure 1.26: 1DOF structure in Cartesian coordinate	29
Figure 1.27: Angle relationship for 1DOF structure: (a) two surface angles as a function of normalized height h ; (b) relationship of two surface angles.....	31
Figure 1.28: Exposure patterns and photomasks: (a) the conceptual design of photomask: patterns with the same colors are patterns on top and bottom polymer films (b) the real photomask	32
Figure 1.29: 1DOF Origami folding process: 1 inward folding; 2 flattening; 3 upward folding; 4 jumping up	34
Figure 1.30: Miura sheet folding pattern, final shape and folding process.....	34
Figure 1.31: New geometry for more accurate analytical and numerical models	35
Figure 2.1: Reaction front in the lithiation process[39].....	38

Figure 2.2: Definition of thickness ratio for rod and tube: yellow regions are lithiated silicon Li_xSi ; green regions are pure silicon	39
Figure 2.3: Material boundaries, boundary conditions and temperature fields: green regions are lithiated silicon; gray regions are pure silicon	40
Figure 2.4: Maximum principal stress in nanotube and nanorod: (a) stress contours on deformed shapes during lithiation as a function of thickness ratio; (b) stress values as a function of thickness ratio. The Si nanotube (standard) has a 90 nm outer diameter, and 20 nm thick Si wall. The equivalent Si nanorod (same amount of silicon) has an outer diameter of 74.8 nm. The in situ SEM observation Si nanotube has an 820nm outer diameter, and a 75 nm thick Si wall.....	41
Figure 2.5: Plastic strain in nanotube and nanorod: (a) plastic strain contours on deformed shapes during lithiation as a function of thickness ratio; (b) plastic strain values as a function of thickness ratio	42
Figure 2.6: Setup of analytical solution	43
Figure 2.7: Superposition of ring structure, boundary conditions and continuity requirement....	43
Figure 2.8: Radial stress distribution at different thickness ratio as a function of distance from the tube center: (a) from analytical solution; (b) from finite element method	44
Figure 2.9: Configuration of inner surface from sinusoidal function with $A = 2$, $B=6$ and $C=10$: (a) shape of inner surface; (b) plastic strain distribution of the configuration.....	45
Figure 3.1: Yielding Envelope of Tresca and von Mises criteria in plane stress condition	48
Figure 3.2: Yielding surfaces of two criteria in general cases. <i>Adopted from "Yield surfaces" by Rswarbrick - Own work, based on Yield_surfaces.png. Licensed under CC BY-SA 3.0</i>	49
Figure 3.3: Failure Envelope of Mohr –Coulomb Criterion	50
Figure 3.4: Failure surface of Mohr-Coulomb Criterion in general case[47]	51
Figure 3.5: Theoretical failure envelopes and experimental results of Shirahama sandstone and Yunbari shale: straight horizontal lines are theoretical envelopes[50]	52
Figure 3.6: Theoretical failure envelopes and experimental results of Dunham dolomite [50] ...	53
Figure 3.7: Depth distribution of global seismicity[51][52][53]	53
Figure 3.8: Subducting crust and mantle model	54
Figure 3.9: Volume change at different depth [53].....	55
Figure 3.10: Confining pressure at different depth	56

Figure 3.11: Experimental data on Indian limestone: (a) experimental data and failure criteria by other researcher; (b) internal friction coefficient as a function of depth; (c) inherent stress as a function of depth[49]	57
Figure 3.12: Failure envelope and expected stress curve along depth.....	57
Figure 3.13: Experimental data on different rocks: (a) internal friction coefficient as a function of confining pressure; (c) inherent stress as a function of confining pressure[50]	58

List of Tables

Table 1.1: Parameters for controlled-variable approach.....	20
Table 1.2: Material properties of XL, NXL and PXL Polymers	21
Table 1.3: Pattern length and spacing	24
Table 2.1: Material properties of silicon and lithiated silicon [35][37]	40
Table 3.1: Maximum shear stress calculation	48
Table 3.2: Volume reduction of crust and mantle at different depth [53]	54

Chapter 1 : Self-Assembly of PDMS/SU-8 Films

1.1 Introduction

Self-assembly in general sense can be defined as the spontaneous transformation from single designed building blocks to more complex structures without human intervention[1][2]. It is a very ubiquitous phenomenon in nature, for example self-assembly of protein arrays[3]. Self-assembly has been extensively investigated for its promising application nanoscale fabrication[4][5] and microfluidic study[6][7]. Researchers have developed various ways to trigger self-assembly with capillary forces[5][8][9], epitaxial mismatch strains[10][11], and differences in swelling[12]. Gradient in material properties through thin plates and beams was proposed as another method for self-assembly. Difference in material properties caused by the gradient leads to different volume expansion. The mismatch in expansion results in twisting or folding of the material[7][13]. The gradient can be introduced by ultraviolet exposure by photo-lithographic methods.

Motala and Yuan[14][15] developed a new polymer film with PDMS and SU-8. Two materials were mixed with certain mass ratio. Thin films were fabricated by spincoating. Since SU-8 was a UV sensitive material, the film would have gradients of material properties (swelling ratio in solvents and young's modulus) after UV exposure. Due to swelling ratio difference in Toluene solution, mismatch strain was induced and made polymer films to fold in the solution. It is a promising material for controllable self-assembly because UV exposure can be deliberately controlled by lithographic technology. In order to have better understanding and control on this self-assembly method, an analytical model for folding direction prediction, a computational model for the final shape prediction and basic experimental calibration are essential.

In previous work, Perlitz[16] developed a computational model and an analytical model for final shape prediction. The analytical model adopted solutions of composite laminates experiencing a temperature change from Hyer[17] and Shokrieh[18]. The model used the homogenous and anisotropic assumption for top layer of the polymer films. Effective elastic modulus and effective swelling strain were calculated for the analysis. The model could match results from computational models with respect to swelling strain. However, there was a large difference with

respect to young's modulus. Timoshenko has addressed the bimetal strip bending caused by thermal expansion[19]. However, his solution assumed plane stress and plane strain conditions and was the same for two conditions. In this work, an analytical model based on beam theory and principle of minimum potential energy is developed. Generalized plane strain condition, which is a more accurate approximation, is assumed for the analysis. The model has better agreement with the results from computational models.

Some experimental calibration regarding the radius of curvature and folding angle was carried out for the further application of this self-assembly method. Experiment setup and procedures were adopted from Motala. However, extra UV exposure from natural light was controlled more strictly. It improved the consistency of the experiment. Additionally, cutting fixtures for samples were designed to enhance the efficiency of sample preparation. Based on the calibration results, more complex structures, for example one-degree-of-freedom Origami, were explored and fabricated.

1.2 Analytical model for predicting folding directions

To have a better understanding of this folding mechanism, an analytical model was developed to predict folding directions. Beam theory and principle of minimum potential energy were applied. In this section, the model will be demonstrated and the results will be discussed.

1.2.1 Simplified geometry

Motala and Yuan developed the methods to fabricate the PDMS and SU-8 polymer thin films and introduced material property gradients onto them by UV exposure. The procedures were repeated with better natural light control, which will be illustrated in the subsection 1.3.1. To characterize the geometry of polymer, the samples were immersed in fluorescence solution (Rhodamine 6G 0.1mmol/L) for 12 hours. The material difference in the polymer films gave different absorption of fluorescence solution, which enabled us to visualize the material property gradients under the fluorescence microscope with different light filters. The fluorescence images are shown on Figure 1.1(a) and 1.1(b).

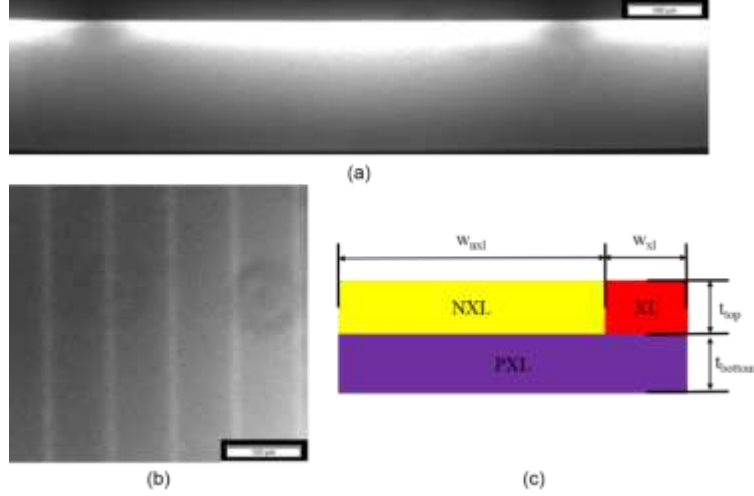


Figure 1.1: Fluorescence images of polymer films and simplified geometry: a) cross-section of 600-micron spacing samples; b) top-view of 100-micron spacing samples (with a different filter); c) simplified cross-section of polymer

From the Figure 1.1(a), a bilayer structure can be seen. The dark parts on the top are UV-exposed parts. Crosslink of the polymer is promoted by SU-8 in these regions. They are denoted as cross-linked regions (XL). The bright parts on the top are shadowed parts. Photomasks block UV exposure on these regions. Crosslink doesn't happen. They are denoted as non-cross-linked regions (NXL). The bottom part has some UV exposure because of scattered UV. Crosslink is promoted by SU-8 partially. This region is denoted as partially-cross-linked region (PXL). From the Figure 1.1(b)¹, a different spacing between XL regions, compared with Figure 1.1(a), can be achieved with a different pattern spacing on the photomasks.

Structure of the polymer is further simplified to what is shown in Figure 1.1(c). Some geometric parameters are defined meanwhile. Thickness of top and bottom layers are denoted as t_{top} and t_{bottom} . Total thickness of the polymer can be controlled by rotating speeds of spincoater. Thickness of each layer is related to UV dose. Width of XL and NXL regions are denoted as w_{xl} and w_{nxl} respectively. Different width are achieved by changing spacing on the photomasks. From the geometry, width of PXL regions can be calculated by

$$w_{pxl} = w_{xl} + w_{nxl} \quad (1.1)$$

¹ A different filter was used. Bright part is XL and dark part is NXL

To calculate the total strain energy, volume of the sample needs to be defined. The length of a sample is defined as 1 for the convenience of calculation.

From the experiments, two folding modes shown in Figure 1.2 have been observed. In the folding mode 1, the top layer wraps up the bottom layer in the direction which XL strips are parallel to the plane where bending is initiated. In the folding molding mode 2, the bottom layer wraps up the top layer in the direction which XL strips are normal to plane where bending is initiated. Both folding modes happened during the experiments. Under certain circumstances, the sample would deform into folding mode 1, open up and finally deform into folding mode 2.

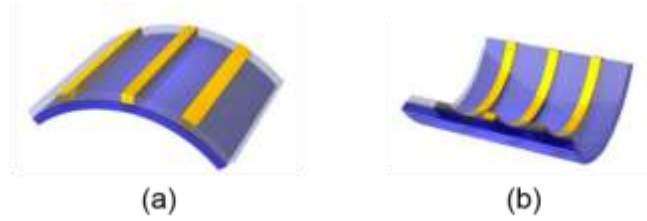


Figure 1.2: Folding modes: a) folding mode 1: top layer wraps up the bottom in parallel direction; b) folding mode 2: bottom layer wraps up the top in normal direction. [15]

A bilayer-beam structure in Figure 1.3 are extracted from two folding modes for the further simplification. By superposition, two folding modes can be achieved from this structure. Potential energy will be calculated corresponding to this configuration.

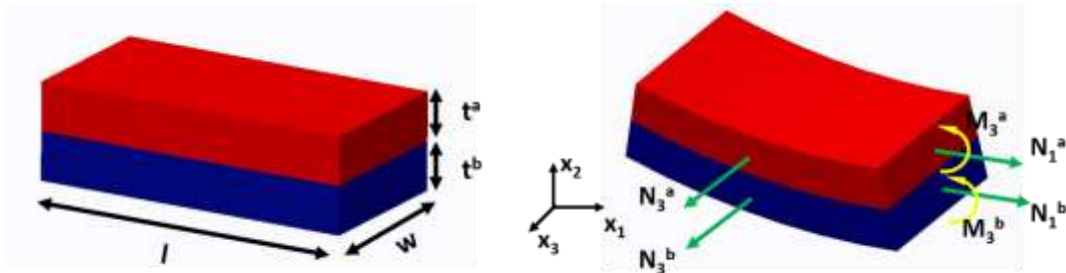


Figure 1.3: Bilayer-beam structure before and after bending

1.2.2 Analytical methods

Based on the simplified geometry, a few assumptions are proposed to make this analytical model compatible with Bernoulli's beam theory and theory of linear elasticity[20]:

- i) Central line, which is a collection of cross-section centroids, is unaltered in length;
- ii) Sectional plane, which is perpendicular to the undeformed centerline, remains plane and perpendicular to the deformed central line;
- iii) Materials are isotropic and linear elastic;
- iv) Radii of curvature are the same for both top and bottom layer;

The first two assumptions are adopted from the basic assumption of Bernoulli's beam theory and the third assumption makes it more convenient for analysis. The fourth assumption is made because thickness of the film (120microns) is small compared to radius of curvature (several millimeters),

The deformed configuration of bilayer beam is shown in Figure 1.3 with annotations. The top layer is denoted as A . The following symbols with super scripts ' a ' are quantities related with top layer. The bottom layer is denoted as B . The following symbols with super scripts ' b ' are quantities related with bottom layer. N_1^a, N_1^b are the equivalent normal traction force in x_1 direction acting at the centroid of x_1 cross-section. N_3^a, N_3^b are the equivalent normal traction forces in x_3 direction acting at the centroid of x_3 cross-section. M_3^a, M_3^b are the coupled moments in x_3 direction. One needs to note that $N_1^a, N_1^b, N_3^a, N_3^b, M_3^a$ and M_3^b are the equivalent forces and moments caused by mismatch strain between two layers. They are not the external traction.

From beam bending and extension equations, we can get stress distribution along the x_1 cross-sections. The stress comes from two parts: stress caused by normal stress N_1 and stress caused by moment M_3 .

$$\sigma_{11}^a = \frac{N_1^a}{A_1^a} - \frac{M_3^a x_2}{I_1^a} \quad (1.2)$$

$$\sigma_{11}^b = \frac{N_1^b}{A_1^b} - \frac{M_3^b x_2}{I_1^b} \quad (1.3)$$

in which A_1^a, A_1^b are x_1 cross-sectional areas and I_1^a, I_1^b are area moment of inertia about x_3 axis. Similarly but without contribution from bending moments, stress distribution along the x_3 cross-sections can be found as,

$$\sigma_{33}^a = \frac{N_3^a}{A_3^a} \quad (1.4)$$

$$\sigma_{33}^b = \frac{N_3^b}{A_3^b} \quad (1.5)$$

in which A_3^a, A_3^b are x_3 cross-sectional areas.

From theory of linear elasticity and the constitutive law, strain components can expressed with stress components together with Young's moduli and Poisson's ratios.

$$\varepsilon_{11}^a = \frac{1}{E^a} (\sigma_{11}^a - \nu^a \sigma_{33}^a) + \alpha^a \Delta T \quad (1.6)$$

$$\varepsilon_{11}^b = \frac{1}{E^b} (\sigma_{11}^b - \nu^b \sigma_{33}^b) + \alpha^b \Delta T \quad (1.7)$$

$$\varepsilon_{33}^a = \frac{1}{E^a} (\sigma_{33}^a - \nu^a \sigma_{11}^a) + \alpha^a \Delta T \quad (1.8)$$

$$\varepsilon_{33}^b = \frac{1}{E^b} (\sigma_{33}^b - \nu^b \sigma_{11}^b) + \alpha^b \Delta T \quad (1.9)$$

in which E^a, E^b are Young's moduli, ν^a, ν^b are Poisson's ratios, α^a, α^b are thermal expansion coefficient, ΔT is uniform temperature change.

From force equilibrium on x_1 and x_3 cross-sections, we can get 2 equations

$$N_1^a + N_1^b = 0 \quad (1.10)$$

$$N_3^a + N_3^b = 0 \quad (1.11)$$

From moment equilibrium about x_3 axis, we can get 1 equation,

$$M_1^a + M_1^b - N_1^a \frac{t^a}{2} + N_1^b \frac{t^b}{2} = 0 \quad (1.12)$$

in which t^a, t^b are the thickness of each layer. By using generalized plane strain conditions, another 2 equations are obtained,

$$\varepsilon_{33}^a = \varepsilon_0 \quad (1.13)$$

$$\varepsilon_{33}^b = \varepsilon_0 \quad (1.14)$$

From the continuity of strain at the interface between top and bottom layer, we can get another equation,

$$\varepsilon_{11}^a|_{x_2=-\frac{t^a}{2}} = \varepsilon_{11}^b|_{x_2=\frac{t^b}{2}} \quad (1.15)$$

From the assumption iv), we have another equation

$$\frac{M_1^a}{I_1^a E^a} = \frac{M_1^b}{I_1^b E^b} \quad (1.16)$$

In the system, we have 7 unknowns $N_I^a, N_I^b, N_3^a, N_3^b, M_3^a, M_3^b$ and ε_0 . We also have 7 equations. The system is solvable. The solution for radius of curvature can be express with Young's modulus ratio and thickness ratio between top and bottom layer. The final expression is

$$R = \frac{h\{-mn(m^4n^2 + 5m^3n + m^2(6n + 4) + m(4n + 6) + 5) + (m^3n + 1)(mnv_b + v_a)^2 - 1\}}{6(\alpha_a - \alpha_b)T(1 + m)^2mn[1 + v_a + mn(1 + v_b)]} \quad (1.17)$$

in which n is the Young's modulus ratio between top and bottom layer, m is the thickness ratio between top and bottom layer, and h is the thickness of entire bilayer structure. Compared with Timoshenko's solution in equation(1.18) [19] for both plane stress and plane strain condition, final expression for generalized plane strain condition are more complex.

$$R = \frac{h\{3(1 + m)^2 + (1 + mn)(m^2 + \frac{1}{mn})\}}{6(\alpha_b - \alpha_a)T(1 + m)^2} \quad (1.18)$$

Some preliminary tests of solution for generalized plane strain condition have been done and shown its better accuracy compared with Timoshenko's solution. The tests will be discussed at the end of this subsection.

Based on the stress and strain distribution, total potential energy can be calculated. The total potential energy are defined as

$$\Pi \equiv \int_V W(\varepsilon) dV - \int_V b_i u_i dV - \int_{S_T} T_i u_i dS \quad (1.19)$$

in which $W(\varepsilon)$ is strain energy density, b_i is components of body forces, T_i is components of external traction. For this problem, no body force or external traction are applied. The potential energy is equal to strain energy. Therefore the potential energy is simplified as,

$$\Pi = \int_V W(\varepsilon) dV \quad (1.20)$$

For linear elastic material, the strain energy density is defined as

$$W(\varepsilon) \equiv \frac{1}{2} C_{ijkl} \varepsilon_{kl} \varepsilon_{ij} = \frac{1}{2} \sigma_{ij} \varepsilon_{ij} \quad (1.21)$$

in which C_{ijkl} is components of stiffness tensor, ε_{ij} is components of mechanical strain (different from thermal strain $\alpha \Delta T$). From the previous discussion, we know no shear stress or strain exist in the system. Since the structure is free x_2 direction, stresses in x_2 direction are zero for both top and bottom layer. The potential energy in terms of stress and strain components is

$$\Pi = \frac{1}{2} \int_V \{ \sigma_{11}^a (\varepsilon_{11}^a - \alpha^a \Delta T) + \sigma_{33}^a (\varepsilon_{33}^a - \alpha^a \Delta T) + \sigma_{11}^b (\varepsilon_{11}^b - \alpha^b \Delta T) + \sigma_{33}^b (\varepsilon_{33}^b - \alpha^b \Delta T) \} dV \quad (1.22)$$

Thermal strain $\alpha^a \Delta T$ and $\alpha^b \Delta T$ are ruled out by the definition of strain energy density.

To verify the solution for generalized plane strain condition, three bilayer beams with common metal materials, steel/aluminum beam, steel/copper beam and copper/aluminum beam, are implemented with finite element methods. Deflection at the end of the beams and strain energy are calculated numerically by FEA and analytically by generalized plane strain solution and Timoshenko's solution. Comparison among three solutions is illustrated in Figure 1.4. From the figures, we can see solutions for generalized plane strain condition is closer to the numerical solutions in both deflection and strain energy. We can conclude that this solution is more accurate than Timoshenko's solution for bilayer beam bending problems. The method for strain energy calculation is also verified to be correct.

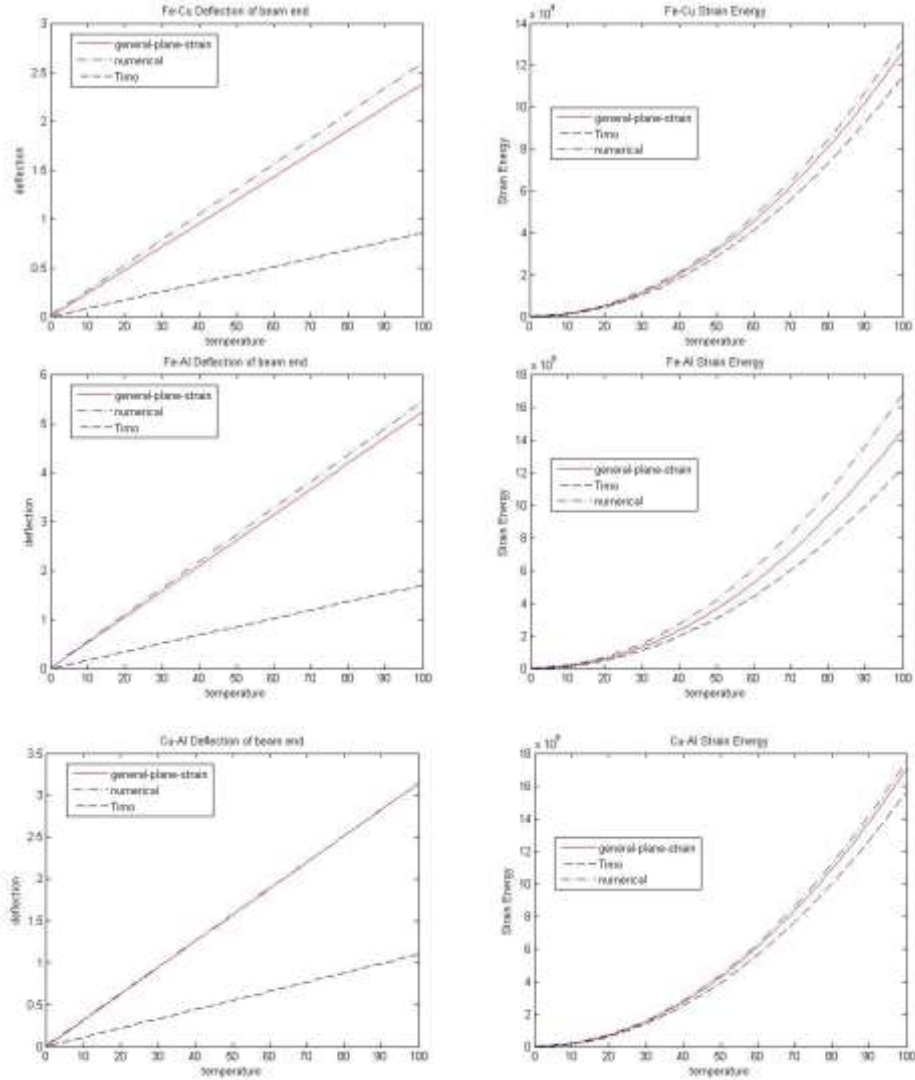


Figure 1.4: Deflection and strain energy comparison between numerical solution, solution for generalized plane strain condition and Timoshenko's solution

To predict the more preferable folding direction, principle of minimum potential energy is applied. By integrating through the volume with respect to two different folding modes, potential energy of two modes can be calculated correspondingly. Principle of minimum potential energy states that the actual displacement field should minimize the potential energy among any kinematically admissible displacement fields. Therefore, the folding mode that gives smaller potential energy is the preferred folding mode.

1.2.3 Results and discussion

For the parametric study effects from material properties, Young's moduli and swelling ratio are normalized by fraction between material properties of cross-linked (XL)/partially-cross-linked (PXL) regions and those of non-cross-linked region as following:

$$E_{xn} = \frac{E_{xl}}{E_{nxl}} \quad (1.23)$$

$$E_{pn} = \frac{E_{pxl}}{E_{nxl}} \quad (1.24)$$

$$\alpha_{xn} = \frac{\alpha_{xl}}{\alpha_{nxl}} \quad (1.25)$$

$$\alpha_{pn} = \frac{\alpha_{pxl}}{\alpha_{nxl}} \quad (1.26)$$

E is the Young's modulus, α is the swelling ratio. Subscripts xl , pxl and nxl stand for XL, PXL and NXL regions. Subscript xn stands for the ratio between XL and NXL regions and pn stands for the ratio between PXL and NXL regions.

From the material properties tested by Motala and Yuan[14][15], default values of E_{xn} , E_{pn} , α_{xn} and α_{pn} were 6.66, 5.01, 0.323 and 0.632. Since young's modulus of XL was greater than that of PXL, E_{xn} was always larger than E_{pn} . Swelling ratio of PXL was greater than that of XL, thus α_{xn} was always smaller than α_{pn} . At the same time, geometric parameters as thickness of each layer and spacing between two XL regions remained the same through the study.

To investigate the effects from swelling ratio of different regions, young's moduli were set to default values. Both α_{xn} and α_{pn} were varied from 0 to 1. Finite element methods were used to generate a scatter plot in Figure 1.5(a) which shows a boundary between two folding modes. The boundary from analytical solution is also drawn on the figure. Similarly, to investigate the effects from young's moduli of different regions, swelling ratios were set to default values. Both E_{xn} and E_{pn} were varied from 1 to 9. The scatter plot from the numerical solution and the boundary from the analytical solution is also plot in Figure 1.5(b)

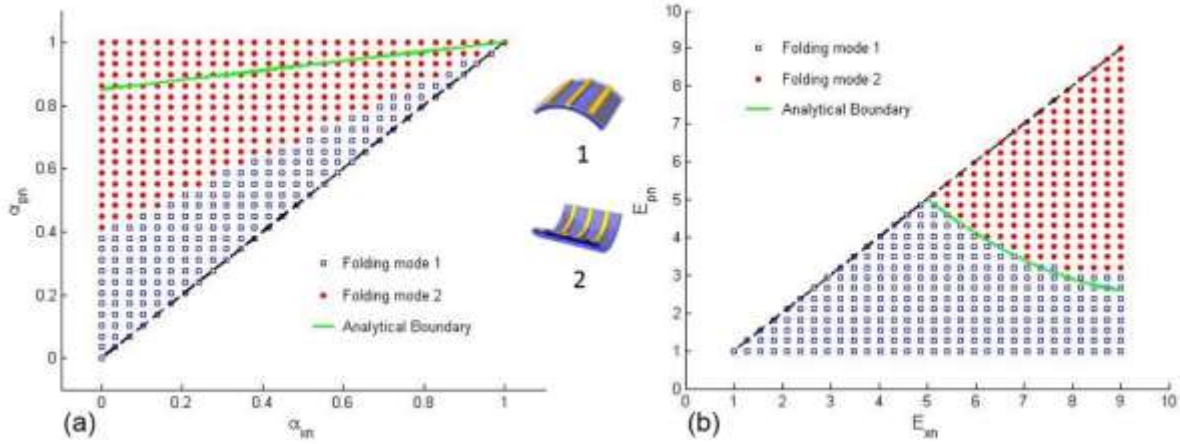


Figure 1.5: Scatter plot and boundaries of two folding modes: a) with respect to swelling ratio with fixed $E_{xn} = 6.66$ and $E_{pn} = 5.01$ b) with respect to Young's modulus with fixed $\alpha_{xn} = 0.323$ and $\alpha_{pn} = 0.632$

A mismatch is found in Figure 1.5(a). The mismatch can be explained with lower strain energy calculated by analytical solution. In the analytical solution, stress and strain caused by interaction between XL/PXL beam and NXL/PXL beam were ignored. In the mathematical expression, the strain energy by two superposed fields can be calculated by

$$U(\varepsilon^1 + \varepsilon^2) = U(\varepsilon^1) + U(\varepsilon^2) + \int_V C_{ijkl} \varepsilon_{ij}^1 \varepsilon_{kl}^2 dV \quad (1.27)$$

in which $\varepsilon^1, \varepsilon^2$ are two strain fields proposed on the body. In the strain energy calculation with analytical solution, the last term from interaction of two fields were neglected because we artificially divided one beam to two different beams. Therefore, the calculated strain energy for both folding modes was lower than the real value. Since the interaction between two beams was not addressed in the analytical solution, deduction in strain energy could not be evaluated.

To get better understanding of effects from material properties, young's modulus and swelling ratio of each region were modified to see changes of the boundary between two folding modes. Young's modulus of XL was modified by varying E_{xn} from 1 to 10 and properties of other materials remained the same. Similarly, young's modulus of PXL was modified by varying E_{pn} from 1 to 10 and properties of other materials remained the same. Changes of the boundary are illustrated in Figure 1.6(a) and (b) respectively. Above the boundary is the folding mode 1. From

the figure, we can conclude that increasing young's modulus of XL or PXL relatively with respect to NXL will make folding mode 1 more preferable at the lower swelling ratios of XL and PXL.

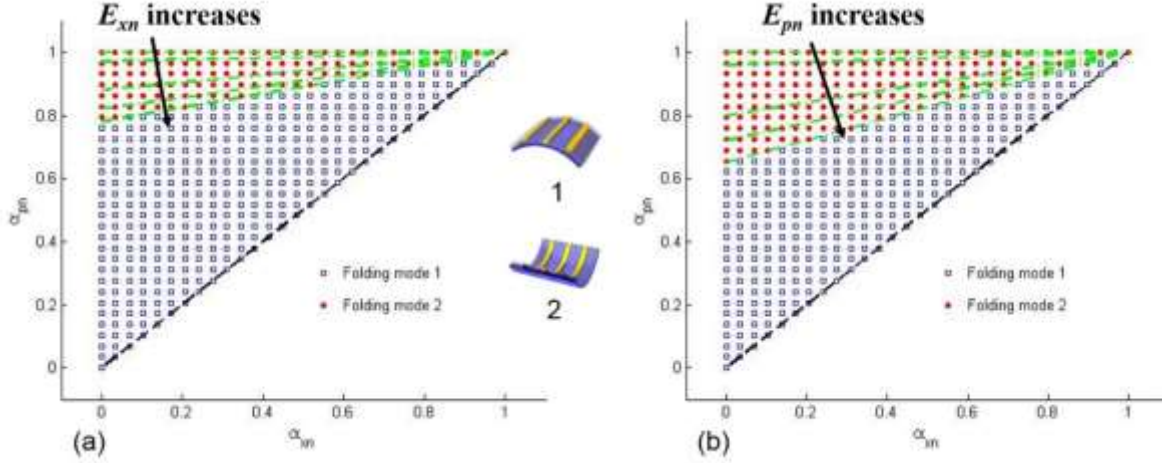


Figure 1.6: Changes of boundaries between two folding modes with different E_{xn} and E_{pn} : (a) increasing E_{xn} from 1 to 10 with $E_{pn} = 5.01$; (b) increasing E_{pn} from 1 to 10 with $E_{xn} = 6.66$

In the similar way, swelling ratio of XL was modified by varying α_{xn} from 0 to 1 and properties of other materials remained the same. Swelling ratio of PXL was modified by varying α_{pn} from 0 to 1 and properties of other materials remained the same. Changes of the boundary are illustrated in Figure 1.7(a) and (b) respectively. Above the boundary is the folding mode 1. From the figure, we can conclude that increasing swelling of XL relatively with respect to NXL will make folding mode 2 more preferable at the lower young's moduli of XL and PXL. However increasing swelling of PXL relatively with respect to NXL will make folding mode 1 more preferable at the lower young's moduli of XL and PXL.

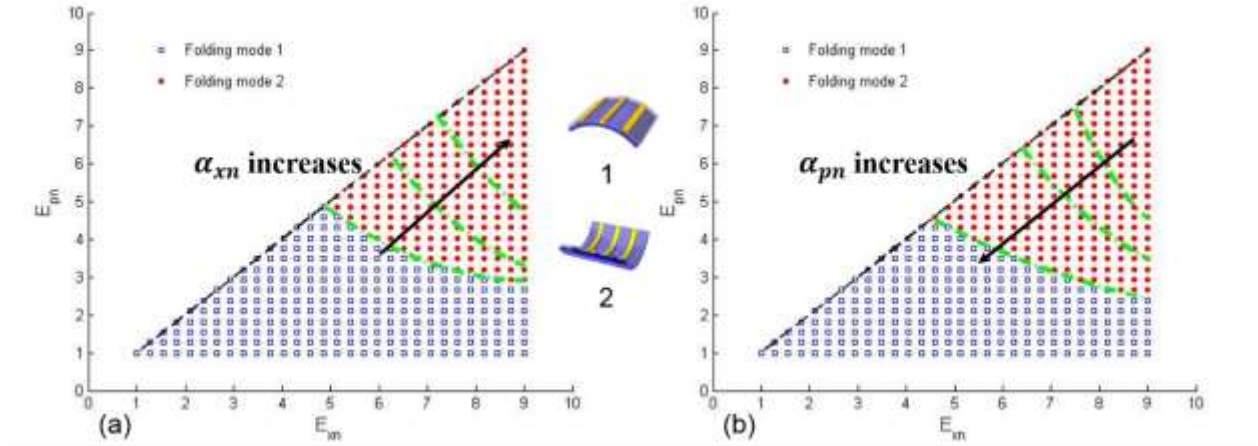


Figure 1.7: Changes of boundaries between two folding modes with different α_{xn} and α_{pn} : (a) increasing α_{xn} from 0 to 1 with $\alpha_{pn} = 0.632$; (b) increasing α_{pn} from 0 to 1 with $\alpha_{xn} = 0.323$

1.3 Experimental calibration of radius of curvature

PDMS/SU-8 films were fabricated to do calibration of radius of curvature. In this subsection, fabrication procedures and experimental setup will be introduced in details. Calibration results will be demonstrated and discussed.

1.3.1 Sample fabrication

Polymer films were fabrication with PDMS and SU-8 mixture. After UV exposure with a mask aligner and a photomask, films with patterns were cut by cutting fixtures to make final samples. First, a plastic Petri dish was placed on a scale and a certain mass of PDMS base, say 14 grams, was added; then curing agent of PDMS was put into the dish with 1:10 mass ratio, for example 1.4 grams curing agent for 14 grams PDMS base; after that SU-8 25 was added with 30% total mass of mixture, say 6.6 grams SU-8 for 22 grams mixture; next three chemicals PDMS base, curing agent and SU-8 were stirred with a mixer for 10 minutes until the mixture was uniform and showed milky color. Finally, the mixture was put into a vacuum chamber to remove bubbles inside for 30 minutes. Mixture before and after stirring and after degassing is shown in Figure 1.8. Aluminum foil was used on top of petri dish to prevent UV exposure from natural light.

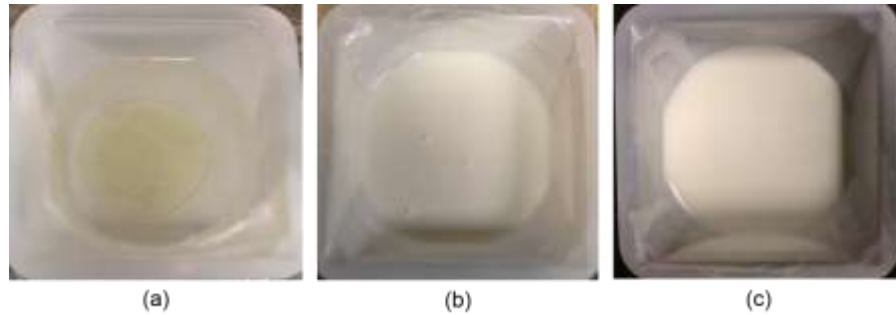


Figure 1.8: Mixture of PDMS/SU-8 at different steps: (a) mixture before stirring; transparent liquid is the PDMS; yellow liquid is SU-8; (b) mixture after stirring; mixture turns to be milk white; bubbles present on the surface; (c) mixture after degassing; bubbles are removed by vacuum. Mixture is in a disposable plastic petri dish

After mixture was made, it was coated onto glass slides to make thin films. First, Kapton tapes was put onto glass slides. Polymer films were easier to be peeled off with Kapton tapes on glass slides. Kapton tapes were chosen because they could survive high temperature during curing and post baking. To prevent bubbles between the glass slides and tape, we used the back of a single-side razor blade to push against the tape when we applied the tape on the glass slides. Then spincoater was set to be 1500 rpm for the coating speed and 30 seconds for coating time. The glass slide was placed on the spindle of spincoater with the middle at the center. After that, the mixture was poured onto glass slides. The spincoater was turned on and the mixture spread out uniformly. Glass slide preparation, distribution of mixture before spincoating and final glass slides are demonstrated in Figure 1.9.

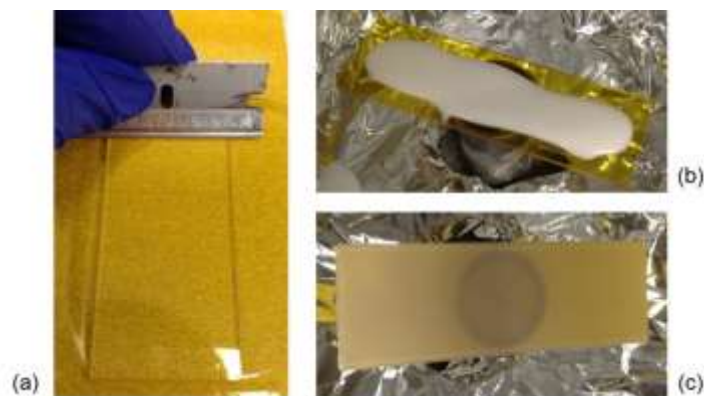


Figure 1.9: Glass slides at different process: (a) apply Kapton tape on the glass slide; back of a razor blade pushes against glass slides to remove bubbles; (b) mixture distributed on glass slides; center and two ends of glass slides have mixture; (c) glass slide with thin film after spincoating

Next, one piece of paper towel was placed onto a glass petri dish. The paper towel was used to prevent glass slides stick onto the petri dish after curing. Glass slides were placed onto the paper towel with two tweezers. Aluminum foil covered the petri dish to block natural lights again. Finally, five glass slides were placed in a petri dish covered with aluminum foil. The glass petri dishes were sent into a curing oven for two-hour curing at 75 degrees Celsius. The glass petri dish is shown in Figure 1.10 at different steps.

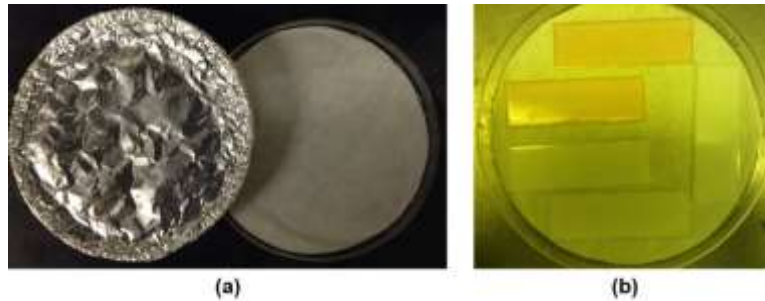


Figure 1.10: Glass petri dish: (a) empty dish with aluminum cover on the left and paper towel inside; (b) dish with 5 samples inside after curing; the picture was taken in cleanroom

After two-hour curing, PDMS/SU-8 samples were transferred to cleanroom for UV exposure. First, a photomask was attached to a mask holder which had a 60mm*60mm exposure window by vacuum. On the photomask, seven different patterns were designed. They all had 10-micron-width slots but different spacing between two slots, 30, 60, 100, 150, 200, 400 and 600 microns respectively. Then one glass slide with polymer film on top was aligned with the photomask according to alignment marks. Disposable tapes were used to keep glass slides attached to the photomask. After that, a chuck inside the mask aligner was removed. Otherwise the chuck would push glass slides again the photomask and break the mask. The mask holder, together with the photomask and glass slide, was assembled onto the mask aligner. Next, energy channel with 10mW/mm² energy density was chosen. Exposure time was set to be 45 seconds. UV exposure was carried out accordingly. Finally, the exposed samples are placed onto an oven at 110 degree Celsius for post baking. Cutting fixtures, which are shown in Figure 1.11, were used to make polymer films into samples. Glass slides were assembled onto the alignment board at the bottom of fixtures. After the punch, cuts were made onto films. With two punches from two fixtures, samples were made and left on the glass slides for the experiments. Sample cutting was done in cleanroom to prevent exposure from natural lights.

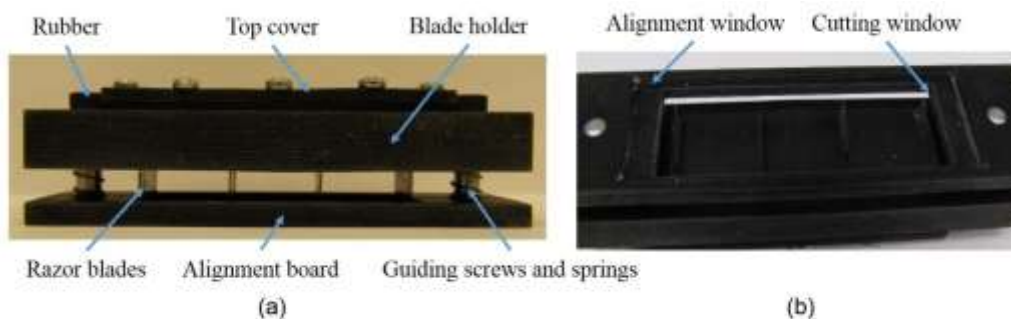


Figure 1.11: Sample cutting fixture: (a) front view of the fixture; (b) bottom view of the fixture

1.3.2 Experimental setup and image processing methods

Experiment setup is shown in the Figure 1.12. A camera on the tripod was set close to a fume hood. To avoid distortion caused by curved surface of the beaker, a beaker with a diameter of 25mm was chosen because the largest dimension of samples was 20mm. At the bottom of the beaker, a quarter coin was deposited together with PDMS as a benchmark for calibration. To have the same height as the camera, the beaker was placed on a plastic bottle. A piece of black rubber was placed behind the small beaker to make better contrast. Toluene was added to the beaker.

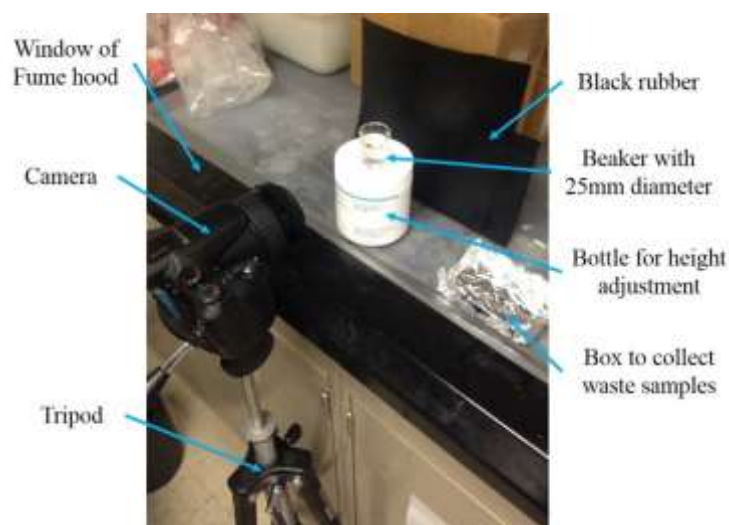


Figure 1.12: Experiment setup for radius of curvature calibration

To carry out the experiment, the camera was turned on to start taking a video first. Then one sample was peeled off from the glass slide with tweezers and put into the toluene solution immediately to avoid exposure from natural lights. After that, the camera recorded deformation of the sample

inside toluene. Finally, a photo of the final profile of the sample was taken for the measurement and calibration. Photos of final profiles are illustrated in Figure 1.13.

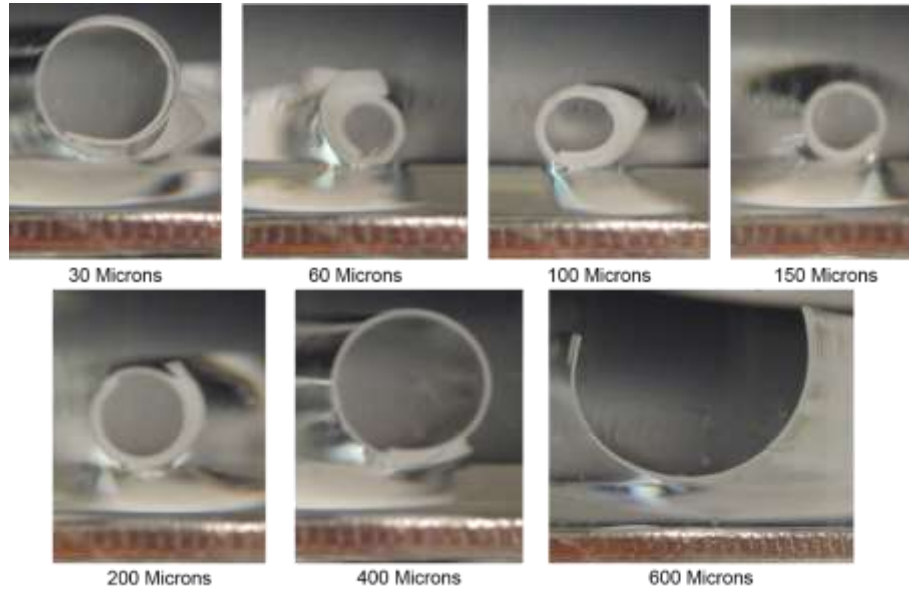


Figure 1.13: Final profiles of samples with different XL spacing in the toluene

Images of final profiles were processed by ImageJ. First, a vertical line was drawn from the top surface to the bottom surface of the coin to measure the thickness. The measurement was in the unit of pixel. Since we had known the thickness of the coin in millimeter, the conversion between two units was established in the software. Then a circle was drawn to fit the circular cross section of the final profile. The radius in pixel was obtained. The calibration procedures were illustrated in Figure 1.14(a). Finally, the radius in pixel was converted to millimeter with the conversion established by coin thickness calibration.

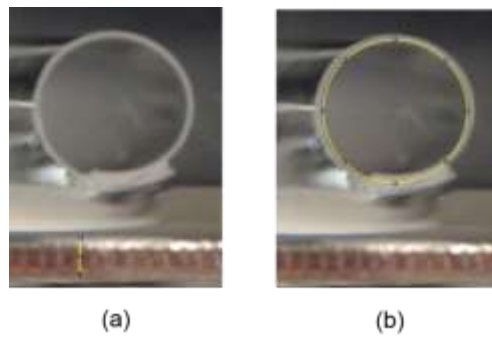


Figure 1.14: Image processing procedures: (a) vertical line for pixel and millimeter conversion; (b) diameter calibration by circular fitting

1.3.3 Results and discussion

Diameters were obtained by image processing and are scattered in Figure 1.15(a). When spacing between two XL regions are small, say less than 100 microns, correlation between diameter and spacing is not well established. The smallest diameter presents at the spacing of 60 microns. However, when the spacing is greater than 100 microns but less than 600 microns, it shows a monotonic increasing correlation between spacing and diameter. In the figure, blue error bars show variation and mean values. We can also notice that, the larger diameters have greater variation. For further exploration of polymer films, pattern spacing between 100 microns and 200 microns are recommended.

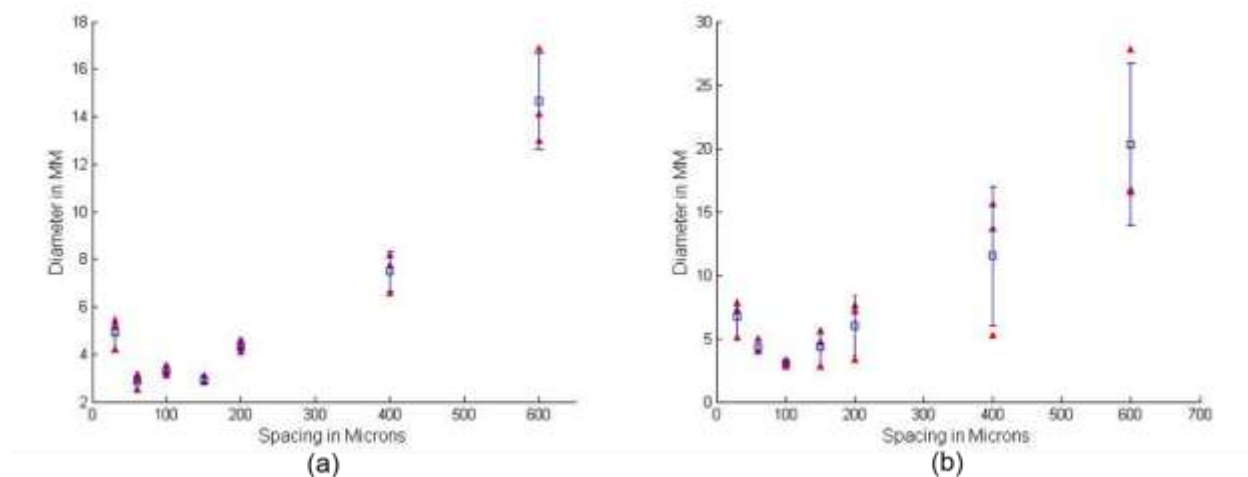


Figure 1.15: Spacing and diameter scattering with 30%wt SU-8: (a) with Aluminum cover during curing process (b) without Aluminum cover during curing process

The variation came from both fabrication and measurement. Firstly, natural UV exposure caused variation in the material properties. Extra natural UV exposure presented during the fabrication and testing. PDMS and SU-8 were mixed and spincoated in a normal laboratory. When we carried out the experiments, UV could also cause some changes in samples. The variation can be seen from Figure 1.15(b). The samples were cured without aluminum cover, which could block natural UV exposure. Apparent increase in variation presented for all samples with different spacing. Therefore, aluminum cover was necessary to get a consistent results. More consistent results could be expected if all procedures, besides controlled UV exposure, were conducted in a UV-free environment. Secondly, cylindrical beakers were used in the experiment. The curved surface of the beakers magnified the features inside the beakers when we took photos of samples. The curved

surface also made it hard for the camera to focus on the samples precisely. Therefore a container with flat surface would give advantages over beakers. Thirdly, final profiles are not perfectly circular, fitting those profiles with circles caused some errors.

1.4 FEA prediction and experimental calibration of folding angle

Most of shell structures like package boxes, water tanks, and square tubes can be regarded as a combination of surfaces and angles. Flat surfaces are easy to achieve if no pattern is introduced to the polymer film. However, to control the folding angle, delicate pattern design and experimental calibration are required. To make more complex structures in the future, the method to control folding angles was explored by changing the exposure geometry. First, FEA models were developed to predict the effects of changing each geometric parameter. Then it found that angles were more controllable by changing the pattern length and pattern spacing. After that, a photomask including different pattern lengths was designed and manufactured. Experiments were carried out to calibrate the relationship between pattern lengths and folding angles. Finally, results from FEA prediction and experiments were compared and discussed.

One simple method is that instead of patterning the entire film, different material properties are only introduced to a narrow strip. The patterned region can achieve curved surface, but unpatterned region will remain flat. Therefore an angular shape can be achieved. The length of patterned region L will be controlled. The conceptual design and expected folding shape are demonstrated in Figure 1.16.

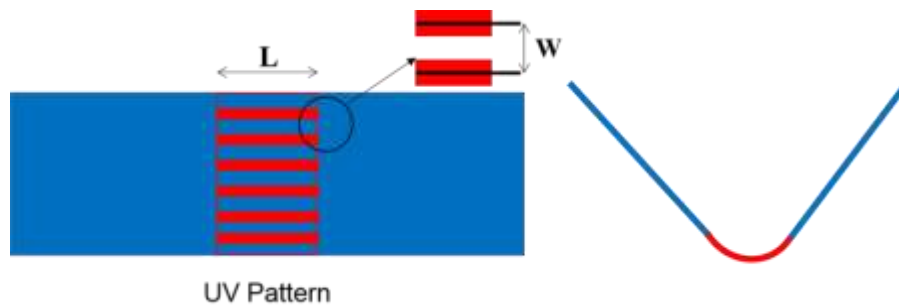


Figure 1.16: Conceptual design and expected folding shape

1.4.1 Preliminary FEA implement

Three geometrical parameters can be varied by changing fabrication methods, length of patterned region (L), spacing between two XL regions (S) and thickness ratio between top and bottom layers (t_{top}/t_{bottom}). Before the real experiments, finite element models were developed to find the parameters which could give the most predictable angular folding behavior.

In the model, length of polymer samples was set to be 20mm, width to be 8mm, and thickness to be 120microns. In previous experiment for calibration of radius of curvature, the most consistent samples had pattern region with length (L) of 16mm, spacing (S) between two XL regions 100 microns, and thickness ratio (t_{top} / t_{bottom}) as 1. Pattern length, spacing and thickness ratio were changed to explore their effects on folding angles respectively. The parameter combination is chosen as shown in Table 1.1.

Table 1.1: Parameters for controlled-variable approach

Pattern Length Study		Spacing study		Thickness Ratio study	
Spacing	100 microns	Pattern Length	1mm	Length	1mm
Thickness ratio	1	Thickness ratio	1	Spacing	100microns
Pattern Length		Spacing		Thickness Ratio	
Sample #1	0.5mm	Sample #1	75 microns	Sample #1	1:2
Sample #2	1mm	Sample #2	100 microns	Sample #2	1:3
Sample #3	1.5mm	Sample #3	150 microns	Sample #3	1:1
Sample #4	2mm	Sample #4	200 microns	Sample #4	2:1

To simulate swelling of polymers in solvent, swelling expansion was treated as thermal expansion because of governing equations for both mechanism were the same, except that swelling expansion was concentration-controlled but thermal expansion was temperature-controlled. After normalization concentration and temperature, the polymer would extend to the final volume which could be achieved by swelling in the solvent, after the temperature was increased by 1 degree Kelvin. Equivalent thermal coefficients was calculated for different materials. Other material properties were measured by experiments. They are demonstrated in Table 1.2.

Table 1.2: Material properties of XL, NXL and PXL Polymers

	Young's Modulus	Poisson's Ratio	Equivalent Thermal Expansion
XL	20MPa	0.499	0.057
PXL	15MPa	0.499	0.176
NXL	5MPa	0.499	0.177

3D shell element was used to build the samples because thickness (120microns) was much smaller than length (20mm) and width (8mm) of polymer film. One quarter of the sample was made since the structure was symmetric. Then the structure was divided into three different regions based on the analytical model discussed in previous sections. Different regions are shown in Figure 1.17 together with boundary conditions. They are NXL material over NXL material in green part, NXL material over PXL material in white part, and XL material over PXL material in red part. Region division was achieved by partition, which required a new sketch on the existing surface. Pattern length and spacing were varied by changing sketches of partition. Sections in ABAQUS were defined as composite shell type. In this way, materials for different layers, layer thickness and layer orientation were defined. Thickness ratio were manipulated by defining thickness of different layers. After sections were defined, they were assigned to different regions correspondingly.

The part was assembled and a general static step was chosen. Boundary conditions were applied as shown in Figure 1.17. X-axis symmetry was applied on left vertical edge and Y-axis symmetry was applied on bottom horizontal edge. Temperature increase of entire structure were applied by pre-defined field. The temperature of whole film was increased by 1 degree Kelvin.

**Figure 1.17: Material sections and boundary conditions of quart of the sample**

Red and white regions were small compared to the green region. However, they had greatest stress and displacement gradients during the process. Therefore mesh density was required to be higher

in red and white regions than that of green region. Instead of choosing a very small size of global seed, edges were seeded respectively. For the short edges of both red and white regions, 4 seeds were added on each of them. For the long edges of red and white regions, the size of seed was chosen to be 0.1mm. Similarly both long and short edges of green regions were seeded with a size of 0.2mm. Quad-domain element shape was chosen and element type was standard linear shell element (S4R). A part of meshed sample is demonstrated in Figure 1.18. The rectangles on the left are meshed on the red and white regions and arbitrary quad shapes are meshed on the green region. In this way, the number of elements were reduced and sufficient mesh density was guaranteed on red and white regions.

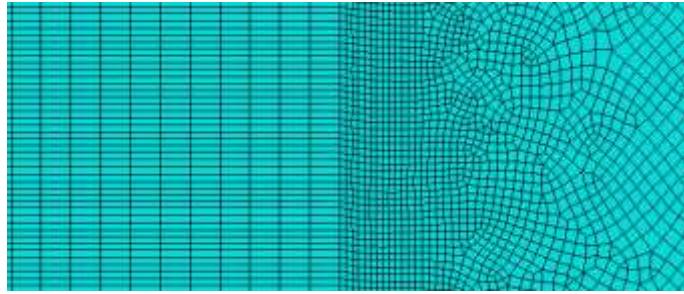


Figure 1.18: Different mesh on different regions on the sample

After meshing, a job was created and submitted. 10 different modes were made in ABAQUS. Some modification in sketch and section parameters were made in accordance with parameters in Table 1.1. Final shapes of 10 different samples were obtained. The results are shown with respect to pattern length, thickness ratio and spacing respectively in Figure 1.19. From the preliminary numerical results, we found that changing pattern length, spacing and thickness ratio gave obvious changes in final angles. However, changing thickness ratio could not be controlled well with UV exposure because there was no sharp material boundaries between XL/PXL and NX/PXL in the real samples. We determined to study the effects from changing pattern length and spacing.

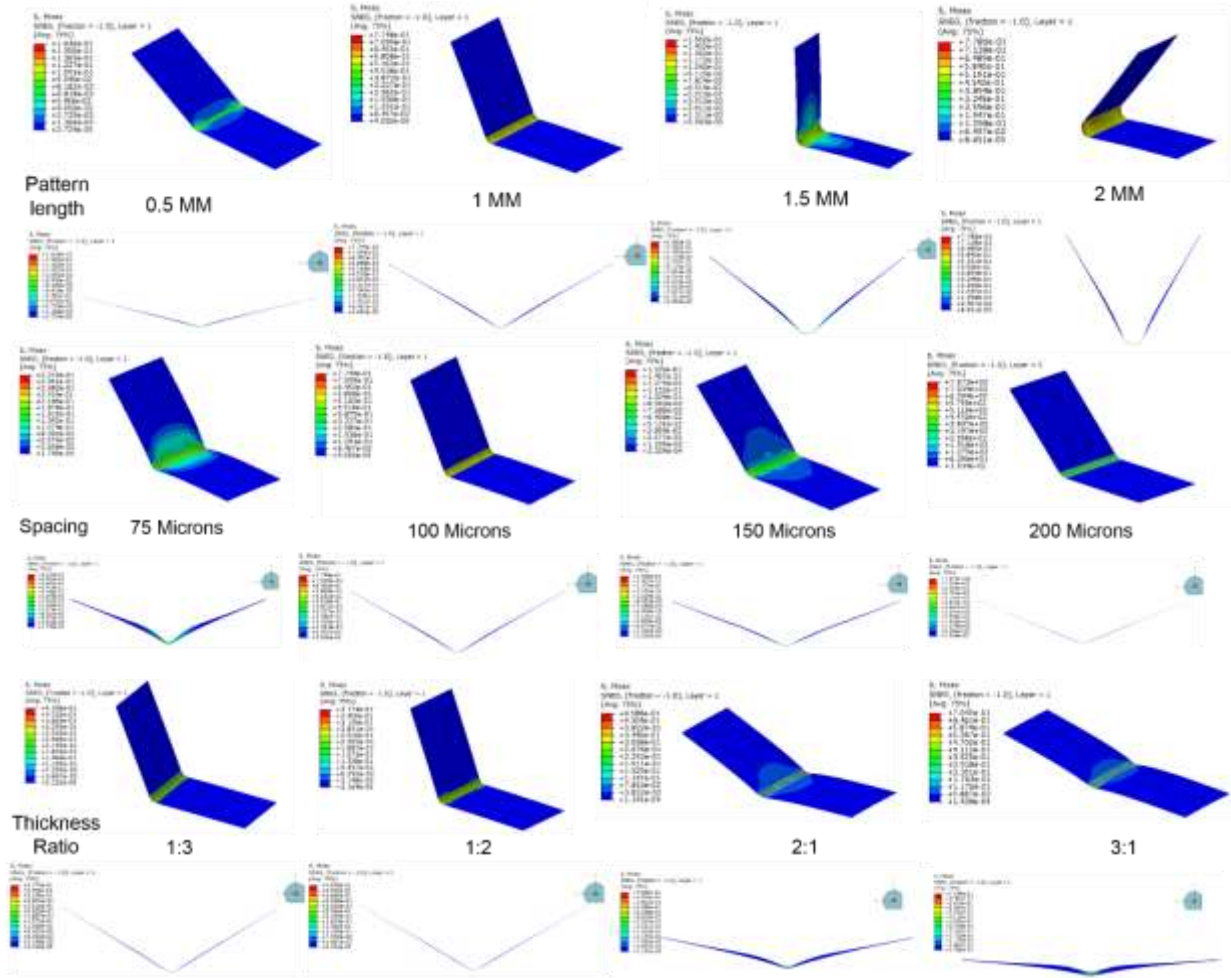


Figure 1.19: Final profiles of polymer samples with different pattern length, spacing and thickness ratio from top to bottom

1.4.2 Sample preparation, experimental setup and image processing

Samples were prepared with the same procedures as described in the subsection 1.3.1 but with a different photomask. The photomask had eight different combinations of pattern length and spacing as shown in Table 1.3. The pattern lengths were chosen in accordance with the diameters calibrated in the subsection 1.3.3.

Table 1.3: Pattern length and spacing

Pattern Number	1	2	3	4
Pattern length (microns)	1962.5	1570	1177.5	785
Spacing (microns)	100	100	100	100
Pattern Number	5	6	7	8
Pattern length (microns)	2616.7	2093.3	1570	1046.7
Spacing (microns)	200	200	200	200

We continued using the previous experimental setup and procedures from the subsection 1.3.2. For each sample, a picture was taken to record the final angle which are shown in Figure 1.20.

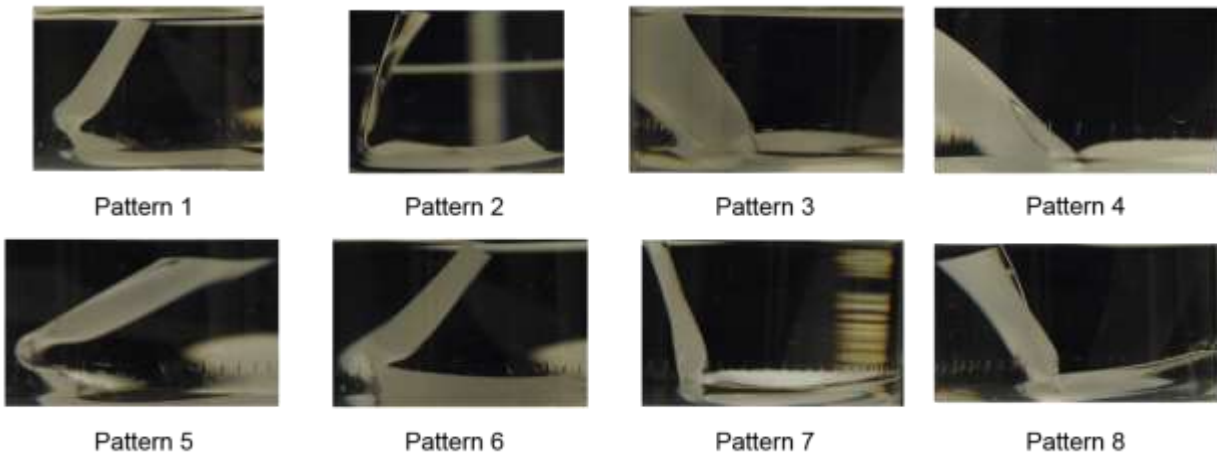


Figure 1.20: Final angles of different patterns

Pictures of final angles were processed by ImageJ for angle measurement as shown in Figure 1.21. For angle measurement, no conversion between pixel and metric units was required.

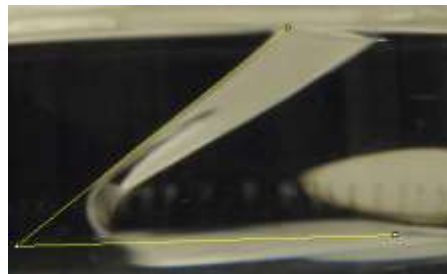


Figure 1.21: Angle measurement in ImageJ

1.4.3 Results and discussion

Pictures of final angles were processed and results were scattered in Figure 1.22 with respect to pattern length at two different spacing 100 microns and 200 microns. Mean and standard deviation were calculated and error bar was added in accordance with two values. Then scattered data were fitted into a linear relation as shown in the figures.

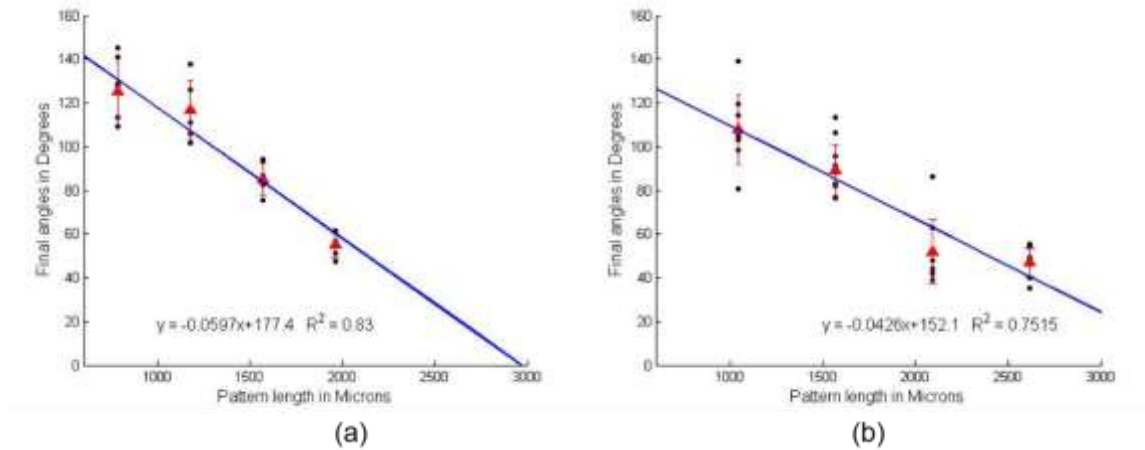


Figure 1.22: Final angles in degrees as a function of pattern length: (a) for 100-micron-spacing; (b) for 200-micron-spacing;

From the figure we can see that for both spacing, final angles decrease with increasing pattern length. However, 100-micron-spacing has a greater decreasing rate than 200-micron-spacing. The linear relationship and different decreasing rate can be understood with the idealized geometry shown in Figure 1.23. AB is an arc at a center O with a radius of r . PA and PB are tangential to the arc at point A and B respectively. In this case, angle θ between PA and PB is the final angle measured in ImageJ.

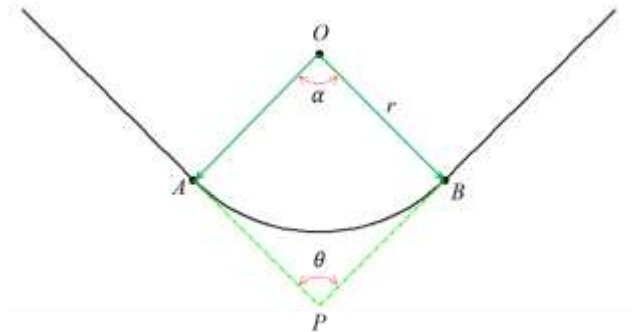


Figure 1.23: Idealized geometry of final angle

For a given radius of curvature r , the angle θ is a function of arc length l and radius r in the following equation. The slope of linear relationship is the negative reverse of radius of curvature.

$$\theta = \pi - \alpha = -\frac{l}{r} + \pi \quad (1.28)$$

In previous subsection of calibration of radius of curvature, 100-micron-spacing samples have a smaller radius (around 1.75mm) than that of 200-micron-spacing samples (around 2.25 mm). If we assume the radius remains the same, the decreasing rate of 100-micron-spacing should be higher and it is consistent with the angular calibration. However, if we applied the calibrated radius to calculate decreasing rate, the corresponding rate for 100 and 200-micron spacing was 0.0327 and 0.0255 degree/micron respectively. The calculated rates were both smaller than the experimental rates, 0.0597 and 0.0426 degree/micron respectively, by 0.017 degree/micron. It meant that calibrated radius was larger than real one. The magnification from curved surface of containers should be the reason for that.

After the experimental calibration was finished, the finite element models were implemented again with different pattern length at 100 and 200 micron spacing. The final angles from finite element models were measured by ImageJ and fitted into a line in the same way. Numerical results were compared with experimental results respectively as shown in Figure 1.24.

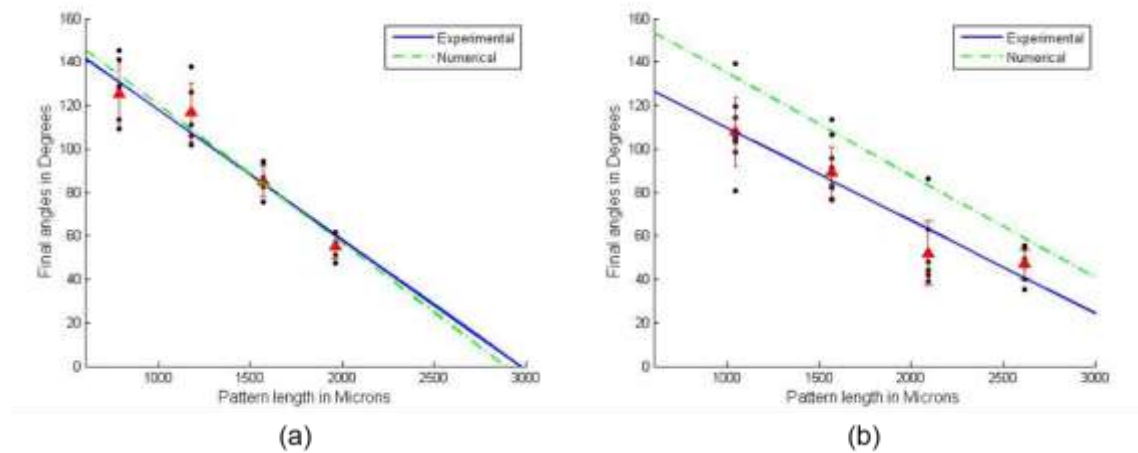


Figure 1.24: Comparison between numerical and experimental results: (a) for 100-micron-spacing; (b) for 200-micron-spacing

For 100-micron spacing, numerical and experimental results matched each other well. However for 200-micron spacing, there was some mismatch. The mismatch came from invalidity of simplified geometry in numerical models. When the spacing between two XL regions increases, PXL regions should be limited to certain regions beneath XL regions instead of the entire bottom layer. Meanwhile, all regions XL, PXL and NXL has material property gradients instead of sharp material boundaries between each other. Numerical model didn't take irregular shapes of material property gradients into consideration, which made it less accurate. However, shapes of material property gradients were difficult to be characterized and implemented in the numerical models.

1.5 Origami with Polymer film

Origami is the traditional art to turn a two-dimensional plane to a three-dimensional structure with crease patterns. The boundary of origami has pushed forwards by mathematical models[21][22][23]. More complex structures can be achieved by origami. The concept of origami has been used in structure design in large scales to solve engineering problems, especially volume restricted problems and multi-structure transformation. Examples include deployable solar panels [24][25], flexible lithium ion batteries [26]and medical stents[27]. Application of origami in engineering gives a new angle to appreciate the traditional art. However, the actuation for the origami in different scales is still a problem for embracing those application. In small scales, the Lorentz forces[28][29], capillary forces[29][30], and different volume expansion[31] in by layer structures have been used for the actuation of origami. We want to apply our polymer films for the origami actuation because crease patterns share the same functionality with exposure patterns in term of folding planes into angles.

Based on the angle calibration of polymer films and crease patterns from origami, more complex three-dimensional structures can be achieved by exposure pattern design. In this subsection, a structure with one degree of freedom (1DOF) as shown in Figure 1.25 were fabricated. A square-shape surface with given edge length was divided into eight regions first with four creases. Red creases and green creases were folded into opposite directions. The angles of creases with the same colors remained the same. By changing one surface angle at one creases, remaining angles would be changed corresponding. If one geometrical parameter were determined, all other parameter were determined at the same time.

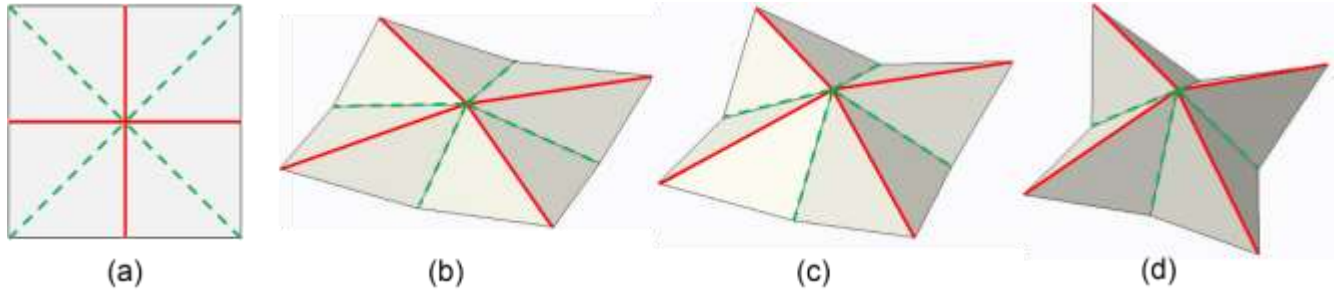


Figure 1.25: One-degree-of-freedom origami structure: (a) crease pattern; (b) (c) (d) structures determined by different surface angles

A mathematical model were developed to explore relationship between surface angles. Exposure patterns were designed to have specific angles in accordance with mathematical relationship. The samples were cut into circular shapes and structures were finally achieved with different surface angles. The results will be demonstrated at the end.

1.5.1 Surface angle relationship

A mathematical model based on three-dimensional geometry was developed to explore the relationship of surface angles in this 1DOF structure. A Cartesian coordinate was built as shown in Figure 1.26. In the model, vertex H is the center of the unfolded square. The other ends of four green creases fall onto one plane xy because green creases are axisymmetric. The normal vector of plane xy through vertex H determines the z axis and origin O . Then we connect the origin with the ends of two green creases A and B to get x and y axis. Next we draw a diagonal line between x and y axis. The diagonal line and line OH determines the symmetric plane of two triangular pyramid $OAPH$ and $OBPH$. Because in each flat surface determined by adjacent red and green creases, the angle between two creases remains to be 45 degrees. That is angle BHP and AHP are always 45 degrees. The location of vertex P is determined in this way. Finally the entire structure are built by mirroring the shape $OAPBH$ by different planes. We need to find the angle between surface AHP and surface BHP , the angle between surface BHP and BHP' and the relationship between two angles.

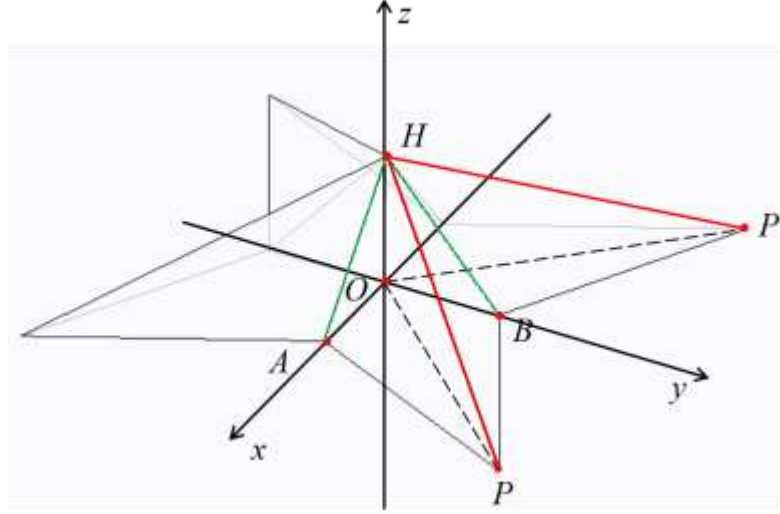


Figure 1.26: 1DOF structure in Cartesian coordinate

For convenience of calculation, the length of edge HB and HA is assumed to be 1, the length of edge HO is h , and the coordinate of vertex P is $(p,p,0)$ because it is on the diagonal line. Then the length of all edges in structure $OAPBH$ can be expressed in terms of h and p as following:

$$HA = HB = 1 \quad (1.29)$$

$$OH = h \quad (1.30)$$

$$OP = \sqrt{2}p \quad (1.31)$$

$$OA = OB = \sqrt{1 - h^2} \quad (1.32)$$

$$AP = BP = \sqrt{\left(p - \sqrt{1 - h^2}\right)^2 + p^2} \quad (1.33)$$

$$HP = \sqrt{h^2 + 2p^2} \quad (1.34)$$

Then the law of cosine is applied in triangle PHB and because angle PHB is 45 degrees,

$$BP^2 = HP^2 + HB^2 - 2HP * HB * \cos \frac{\pi}{4} \quad (1.35)$$

With the above equations, we can find the relationship between p and h . Next the normal vectors of plane HAP , HBP and HBP' are necessary for calculation of surface angles. We suppose the normal vector of plane HAP to be $\overrightarrow{N_{HAP}} = (a, b, c)$ in coordinate form. We have two known vectors in plane HAP .

$$\overrightarrow{HP} = (p, p, -h); \quad \overrightarrow{HA} = (\sqrt{1-h^2}, 0, -h) \quad (1.36)$$

From the properties of normal vectors, we know

$$\overrightarrow{N_{HAP}} \cdot \overrightarrow{HP} = pa + pb - hc = 0 \quad (1.37)$$

$$\overrightarrow{N_{HAP}} \cdot \overrightarrow{HA} = a\sqrt{1-h^2} - hc = 0 \quad (1.38)$$

We can express a and b in terms of c , h and p . Then the normal vector of plane HAP is

$$\overrightarrow{N_{HAP}} = \left(\frac{h}{\sqrt{1-h^2}}, -\frac{h}{p} - \frac{h}{\sqrt{1-h^2}}, 1 \right) \quad (1.39)$$

Similarly we can get the normal vectors of other two planes HBP and HBP' .

$$\overrightarrow{N_{HBP}} = \left(\frac{h}{p} - \frac{h}{\sqrt{1-h^2}}, \frac{h}{\sqrt{1-h^2}}, 1 \right) \quad (1.40)$$

$$\overrightarrow{N_{HBP'}} = \left(-\frac{h}{p} + \frac{h}{\sqrt{1-h^2}}, \frac{h}{\sqrt{1-h^2}}, 1 \right) \quad (1.41)$$

After we get the normal vectors, we can calculate the cosine of surface angles. For surface angle α between plane HAP and HBP , we can get

$$\cos \alpha = \frac{\overrightarrow{N_{HAP}} \cdot \overrightarrow{N_{HBP}}}{\|\overrightarrow{N_{HBP}}\| * \|\overrightarrow{N_{HAP}}\|} \quad (1.42)$$

Similarly, for surface angle β between plane HBP and HBP' , we get

$$\cos \beta = \frac{\overrightarrow{N_{HBP}} \cdot \overrightarrow{N_{HBP'}}}{\|\overrightarrow{N_{HBP}}\| * \|\overrightarrow{N_{HBP'}}\|} \quad (1.43)$$

Given the range of angle α from 0 to 180 degrees and angle β from 90 to 180 degrees, two angles as a function of h is shown in Figure 1.27. The relationship of two angles is also demonstrated in the figure.

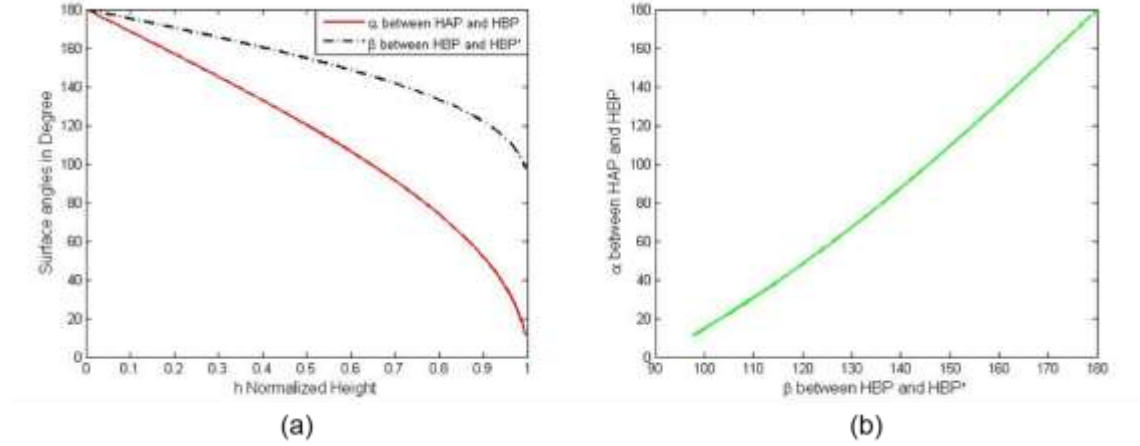


Figure 1.27: Angle relationship for 1DOF structure: (a) two surface angles as a function of normalized height h ; (b) relationship of two surface angles

For both angles, we had problems with singularity in calculation when h got close to 1. The singularity came when we normalized the normal vectors of three planes. However, this problem did not hurt the calculation significantly.

1.5.2 Exposure pattern and photomask design

Red and green creases had the opposite folding directions. Therefore exposure on both sides of polymer samples were required. To have specific folding angles, the exposure pattern was designed according to the angle relationship from the mathematical model and angle calibration results from previous experiments. For one example, if we want to have the surface angle α between surface HAP and HBP to be 120 degrees, we can read from Figure 1.27 (b) that the surface angle β between surface HBP and HBP' should be 155 degrees. Then we want to achieve these two angles with two exposure patterns. We refer to Figure 1.24 and get that the pattern length for 120 and 155 degrees are 982.8 and 421.9 microns at 100-micron spacing pattern. Similarly, we found pattern length for different angle combinations. Finally the patterns for different combinations needed to be placed on a three-inch photomask together with sufficient marks for glass slide alignment.

A photomask is shown in Figure 1.28. It was a 75mm*75mm mask. The edge length of the mask was the same with the length of standard glass slides (75*25mm), which made it convenient for alignment. Exposure patterns were confined within a 60*60mm exposure window because of the

size of mask holders. The exposure window was divided into nine regions. An exposure pattern was placed at the center of each region. Since exposure patterns were required on both sides of samples, alignment between patterns on top and bottom sides was very important. Alignment marks and locations of patterns were deliberately designed. Two patterns with the same color were the patterns on top and bottom sides of the samples. The alignment marks for the two patterns had the same color as the exposure patterns. For one example, green exposure patterns was expected on the sample. First, a glass slide with the polymer film and the mask were aligned for the first time. Four green alignment marks presented at four corner of the glass slide when it was well aligned with the photomask. Then we did the UV exposure on the top side of polymer film. Pattern 1 and pattern 3 would be introduced on two ends of the glass slides. Next, we flipped the glass slide, rotated it about the center by 180 degrees horizontally and aligned it with the mask again. Finally, we did the exposure on the bottom side of polymer film. Because the glass slides was rotated by 180 degrees, regions with pattern 1 on the top would have pattern 3 on the bottom. Similarly, regions with pattern 3 on the top would have pattern 1 on the bottom. In this way, two samples could be made with twice exposure. Alignment between glass slides and the mask was easier by using four alignment marks at the corner only.

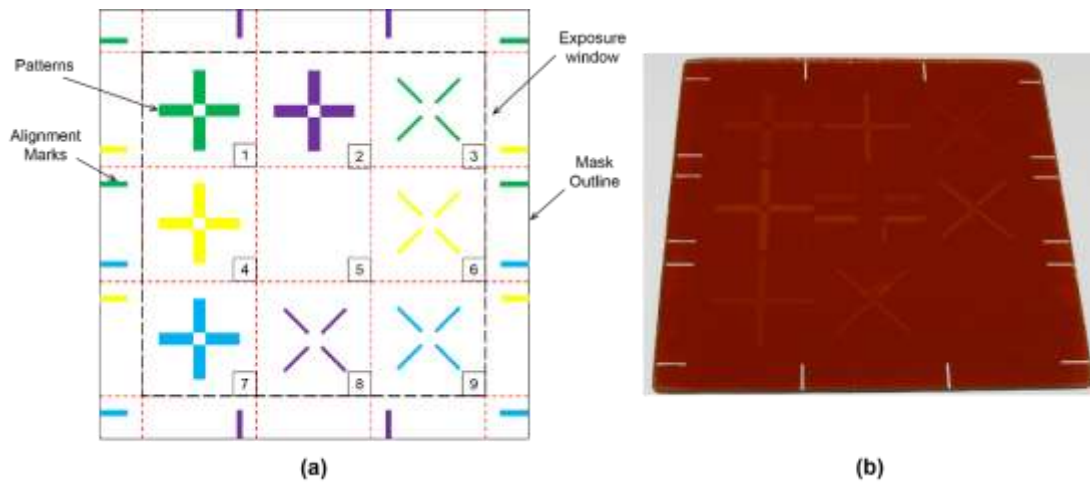


Figure 1.28: Exposure patterns and photomasks: (a) the conceptual design of photomask: patterns with the same colors are patterns on top and bottom polymer films (b) the real photomask

Fabrication procedures and experiment setup were the same as those discussed in subsection 1.3.2 except that transparent tapes were used for the glass slides coating because exposure patterns were required on the bottom of polymer films. After exposure on the top side of samples, glass slides

were flipped and aligned with the mask again to conduct exposure on the bottom side. From experiments, we found that exposure from the top and the bottom did not affect the results, which implied that glass slides and transparent tape did not reduce the UV intensity dramatically. However, the samples were more adhesive to transparent tape than to Kapton tape, which made it more difficult to peel off samples.

1.5.3 Results and discussion

Experimental results were close to our expectation. According to the appearance of samples in the solvents, the folding process was divided into four stages: inward folding (folding mode 1 discussed in subsection 1.2.1); flattening; upward folding (folding mode 2 discussed in subsection 1.2.1); jumping up. Experiments were recorded by a camera. Snapshots of experiment videos were made to show the different stages of folding as shown in Figure 1.29.

The inward folding happened instantaneously as the samples were dropped into the solvents from 0 to 4 seconds. Exposure patterns should give a folding direction parallel to the patterns. Even though we had patterns on the top and bottom sides of samples, inward folding happened only on the top side because pattern width on the top was larger than that on the bottom therefore inward folding on the bottom side was overridden. Then the sample was flattened by itself in the next 6 seconds. After that, exposure patterns gave a folding direction normal to the patterns. The patterns on the top side started folding downwards and the patterns on the bottom side started folding upwards. The folding in this direction lasted about 40 seconds. Finally, the samples were detached with the bottom and jumped up to form a flower shape. The jump up took less than 1 second to finish. The experiment was repeated by different samples with the same exposure patterns and exposure time. Consistency of experiments was verified.

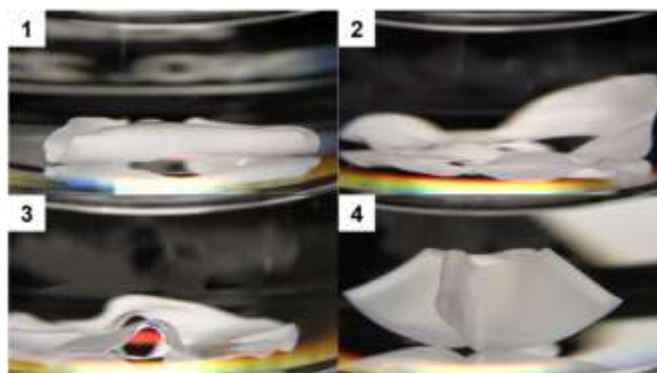


Figure 1.29: 1DOF Origami folding process: 1 inward folding; 2 flattening; 3 upward folding; 4 jumping up

Misalignment of top and bottom patterns was the major source of variance. Glass sides were aligned to the mask according to the alignment marks by hands. Centers of bottom-side patterns could not be aligned with those of top-side patterns perfectly. The typical solution for double-side alignment is the computer-aided system to memorize positions of samples after top-side exposure is finished. Users can align the backside of the samples according to the memorized positions. When we dropped the samples into solvents with tweezers, some part of samples touched the solvent firsts. Swelling was not uniformed across the samples. It was the reason why some part of samples reached the final stages earlier than other part. In some cases, the ununiformed swelling caused the wrong folding directions. In the experiment, we tried to drop samples very quick to minimize this effect. A new device could be developed to release the samples.

Based on the previous analysis and experiments, methods were applied to explore more complex structure like Miura sheet. The crease pattern, final shape and folding process of a real sample is shown in Figure 1.30.

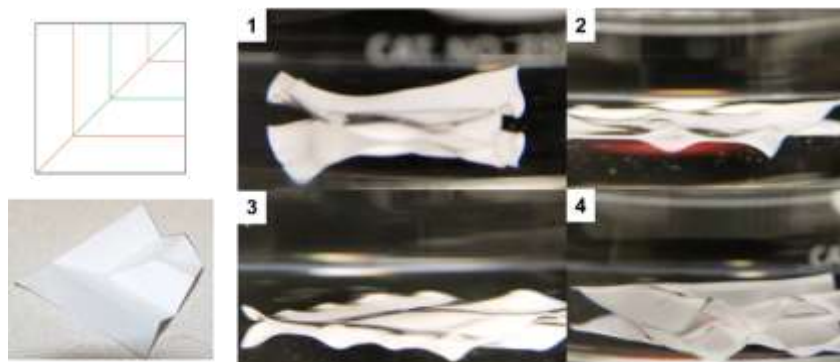


Figure 1.30: Miura sheet folding pattern, final shape and folding process

1.6 Future work

In this work, a simplified geometry of polymer with XL, PXL and NXL regions were used in both analytical model and finite element models. However, the simplified geometry was not always valid for all exposure patterns, especially when spacing between two XL regions are very large. To address this problem, a new geometry model shown in Figure 1.31 was proposed. Instead of assuming the bottom layer as a uniform PXL layer, some NXL regions could present at the bottom layer. The new geometry was more reasonable than the simplified geometry when we increased the spacing. However, the new geometry requires one more parameter, the width of PXL region W_{pxl} . More material property characterization is required to investigate the relationship between W_{xl} and W_{pxl} at different spacing and exposure time. Once the relationship was established, the new geometry could be implemented in both analytical and finite element models. It would enhance the capability of both models to predict behaviors of this polymer film in solvents.

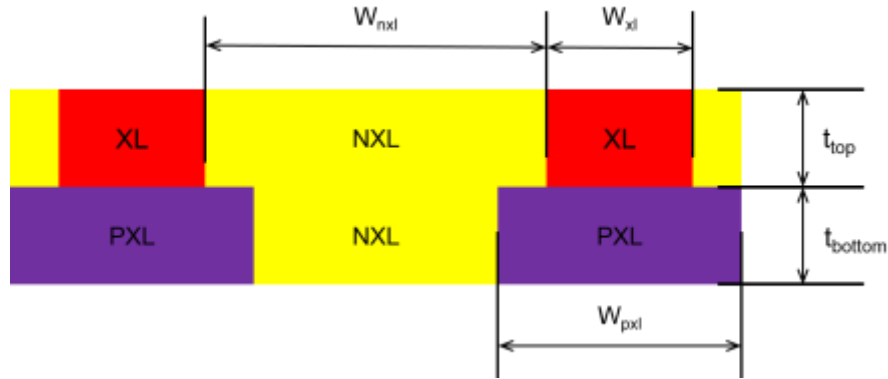


Figure 1.31: New geometry for more accurate analytical and numerical models

Even though the experimental results gave smaller ranges of error than what Motala[14] did, consistence of experiments can be improved. Since the film is sensitive to UV light exposure, experiments can be carried out in a UV-free environment. A cleanroom for nanolithography might be a good place. Or one can find some UV-light filters and cover all light sources in one room to reduced extra UV exposure. Cyclic tests of samples can also be performed in a UV-free environment. Samples were disposed after the experiment currently. If experiments were conducted in a UV-free environment, samples could be soaked and dried for several cycles without material property changes caused by UV lights. One can observe the changes caused by cyclic soaking, which is important for future application.

This polymer film has two opposite folding directions. The two folding directions can be transited. However, experimental work had mainly focused on the final folding directions of samples. Unstable folding directions and transition between two directions were not well studied. The transition happened very fast in Toluene because swelling ratio was high. If one wanted to observe the transition with more details, other solvents with smaller swelling ratio, such as 2-Butanone and Ethyl acetate[14], were recommended to slow down the transition.

Chapter 2 : Failure of Silicon Anodes in Lithium Battery

2.1 Introduction

Current lithium batteries consist of graphite anodes, metal cathodes and lithium ion electrolyte. The battery is rechargeable. When the battery is charged, lithium ions go from metal cathodes to anodes. The anodes are lithiated. When the battery is discharged, lithium ions go from anodes to cathodes. The anodes are delithiated.[32][33] Since lithium has a low molar mass 6.94g/mol, it gives higher energy density compared to other rechargeable batteries, for example lead-acid battery for automobiles. Most portable electronic devices are using lithium battery because of its large energy density. However, energy density is still a limit for application like electric vehicles.[32] Long charging time of the battery is another limit for the board application. Lithium battery with higher energy density and shorter charging time has been expected and investigated extensively.

One promising way to enhance the energy density to use silicon instead of graphite as the anodes because silicon has the highest known theoretical charge capacity, which is more than 10 times of that of graphite.[34][35] However, silicon has up to 300% volume expansion after lithiation. If we continued using the structure of graphite anodes, expansion of silicon would introduce mismatch strain and stress between silicon and substrate. [34][35][36][37] The stress would finally lead to fracture of silicon and functional failure of the anode. To reduce stress and avoid fracture, a nanorod structure was proposed by Cui[34]. The distance between rods were designed and allowed silicon to expand during the lithiation without causing fracture. Liu[38] proposed a nanotube structure recently. The nanotube was fabricated with the same amount of silicon. But it had both inner and outer surface. Shorter charging time was expected for the larger surface/volume ratio. When nanotube structures were tested, shorter charging time was verified. Another interesting result was that nanotube structures could sustain larger number of charging-discharging cycles before fracture happened. It means the nanotube structure gives some advantages in mechanics over the nanorod structure.

To investigate the failure of silicon anode caused by mismatch strain and stress, a finite element model has been developed. An analytical model based on theory of elasticity helps to verify the

necessity of finite element model. In this chapter, numerical and analytical models will be demonstrated. For the future development of silicon anodes, a configuration described by a sinusoidal functions will be presented at the end.

2.2 FEA model for stress and strain evolution

2.2.1 FEA implement

Lithiation process and material properties of lithiated silicon were studied by literature review. Lithiation process is a reaction-rate controlled process[33][39][40][41]. Lithium ion is always sufficient for the reaction. A reaction front between lithiated silicon and pure silicon is found experimentally, which is shown in Figure 2.1. Compared to the diameters of nanorod (37.4nm) and nanotube (inner 25nm and outer 45nm), thickness of reaction front, which is around 1nm, is negligible. It can be considered as a material boundary between lithiated and pure silicon. Furthermore, the lithiation process can be regarded as changing locations of material boundary from the surfaces to the core of anodes. Only two sets of material properties were required for the presence of material boundary. One set was for pure silicon and another for lithiated silicon. From the previous tests by other researchers, lithiated silicon is a ductile material with yielding stress of 500MPa. [37][40][42][43] In models by other researchers, lithiated silicon was assumed to be linear elastic and perfectly plastic.

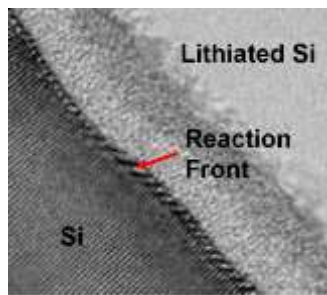


Figure 2.1: Reaction front in the lithiation process[39]

Difference of the nanorod and nanotube comes from the cross-sections. Instead of modeling three-dimensional structures, two dimensional models of cross-sections were developed. Since both cross-sections are symmetric, only a quarter of cross section was used in the model. 2D planar part was chosen in Abaqus with deformable shell features. The inner and outer radii of nanotube

were adopted from the experiment. They were 25nm and 45nm respectively. An equivalent nanorod had an outer radius of 37.4nm to have the same amount of silicon. To determine locations of material boundary, a non-dimensional value, thickness ratio was defined as shown in Figure 2.2.

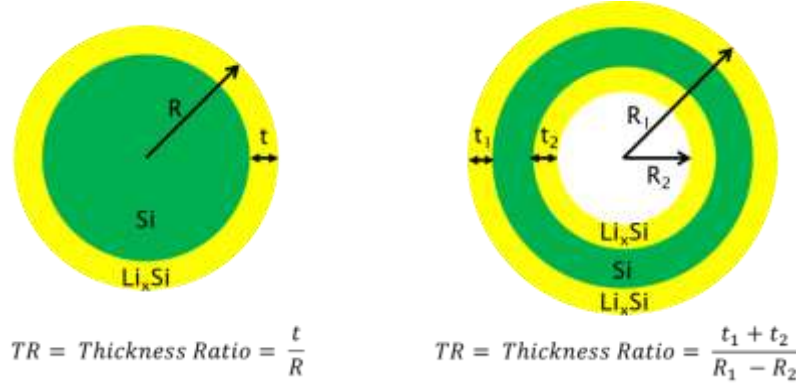


Figure 2.2: Definition of thickness ratio for rod and tube: yellow regions are lithiated silicon Li_xSi ; green regions are pure silicon

Even though reaction rates are different in different crystalline directions, the same reaction rate was assumed because amorphous silicon was used for fabrication. Radius of rod was known, locations of material boundary could be easily determined with thickness ratio. Inner and outer radii of tube were known. One more equation was required to find thickness of lithiated silicon on both sides. From the assumption of the same reaction rate, the same amount of silicon is lithiated on both side. In this case, the area of inner and outer lithiated silicon rings was the same. Therefore we had

$$\pi[R_1^2 - (R_1 - t_1)^2] = \pi[(R_2 + t_2)^2 - R_2^2] \quad (2.1)$$

With this equation, locations of material boundaries was determined on both sides of pure silicon. By surface partition, material boundaries are implemented which is shown in Figure 2.3. Two different material pure silicon and lithiated were defined with parameters in Table 2.1 and assigned to corresponding regions. The volume expansion was treated as thermal expansion. Expansion coefficient was determined to match 300% volume expansion after lithiation. By increasing 1 degree Kelvin, a unit volume of lithiated silicon ($1 \times 1 \times 1$ cube) would achieve the final volume of $(1 + 0.6)^3 \approx 4$.

Table 2.1: Material properties of silicon and lithiated silicon [35][37]

	Silicon	Lithiated Silicon
Behavior	Linear elastic	Linear elastic perfectly plastic
Young's modulus	80GPa	15GPa
Poisson ratio	0.22	0.17
Yielding stress	-	0.5GPa
Expansion Coefficient	0	0.6

Boundary conditions for both rod and tube are symmetric conditions on vertical and horizontal edges of the cross sections. It was easy to implement symmetric boundary conditions. It was another reason to choose a quart of cross section in the model. A uniform temperature field of 1 degree Kelvin was applied. Material boundaries, boundary conditions and temperature field are demonstrated in Figure 2.3.

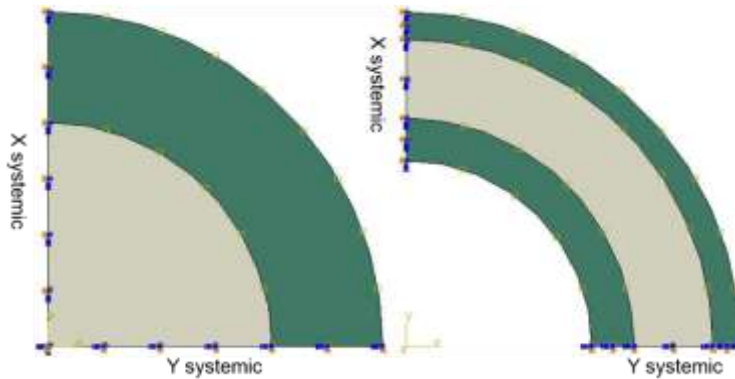


Figure 2.3: Material boundaries, boundary conditions and temperature fields: green regions are lithiated silicon; gray regions are pure silicon

The part was meshed with linear quad elements. Different mesh density was chosen for pure silicon and lithiated silicon regarding to their geometrical dimensions. Plane stress condition was chosen for both structure for the convenience of von Mises stress comparison.

2.2.2 Results and discussion

Lithiated silicon was assumed to be linear elastic and perfectly plastic. When von Mises stress in the lithiated silicon is greater than yielding stress (0.5GPa), plastic deformation occurs and von Mises stress remains to be 0.5GPa for the assumption of perfectly plasticity. Fracture won't happen

until the plastic strain reaches the ultimate strain of the material. However, pure silicon is brittle material. When maximum principal stress overpasses the ultimate tensile stress (around 7GPa), fracture will occurs. Failure of lithiated silicon is related with plastic strain and failure of pure silicon is related with maximum principal stress. Therefore, two quantities are compared respectively.

Maximum principal stress evolution during the lithiation process is illustrated in Figure 2.4. Color bars are different for nanotube and nanorod. For both structures, maximum stress happens at the pure silicon regions. The maximum value of nanotube is greater than that of nanorod. However, the highest maximum principal stress in the pure silicon is below ultimate tensile stress in both structures. This is consistent with experimental observation that no cracks were present during the first lithiation cycle.

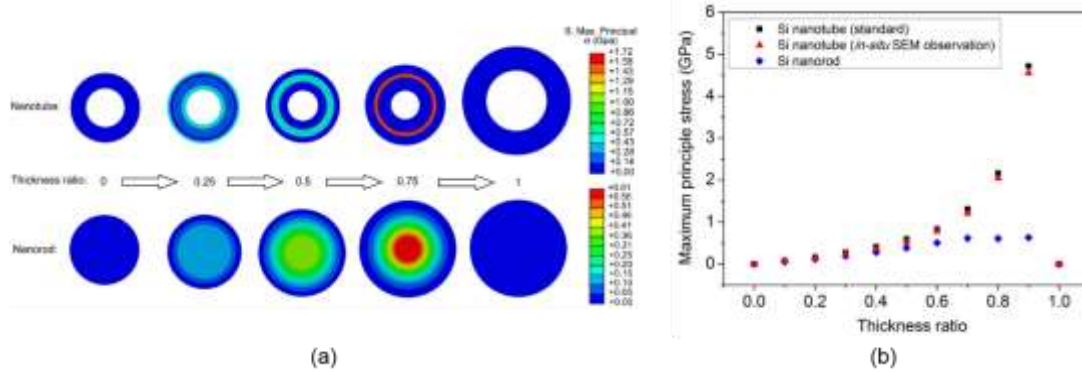


Figure 2.4: Maximum principal stress in nanotube and nanorod: (a) stress contours on deformed shapes during lithiation as a function of thickness ratio; (b) stress values as a function of thickness ratio. The Si nanotube (standard) has a 90 nm outer diameter, and 20 nm thick Si wall. The equivalent Si nanorod (same amount of silicon) has an outer diameter of 74.8 nm. The in situ SEM observation Si nanotube has an 820nm outer diameter, and a 75 nm thick Si wall.

Plastic strain evolution is illustrated in Figure 2.5. For both structures, maximum plastic strain happens at the interface between lithiated and pure silicon. When thickness ratio is smaller than 0.6, plastic strain in both structures increases gradually. When thickness ratio is larger than 0.6, plastic strain in nanorod increase dramatically. However, no obvious increase of plastic strain happens in nanotube structure. More plastic strain was accumulated in rod structure after each lithiation cycle.

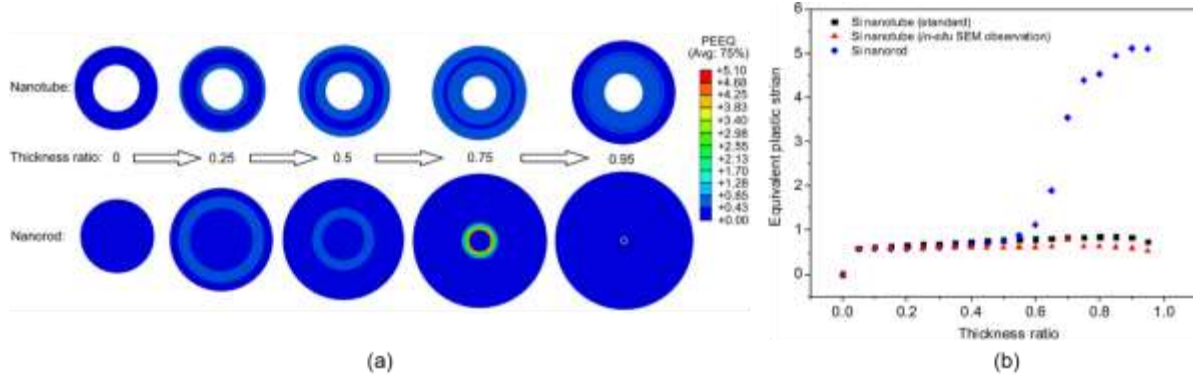


Figure 2.5: Plastic strain in nanotube and nanorod: (a) plastic strain contours on deformed shapes during lithiation as a function of thickness ratio; (b) plastic strain values as a function of thickness ratio

Failure of two structures can be explained by low-cycle fatigue theory, which applies to total cycle to failure fewer than 10^3 . Low cycle fatigue is governed by the empirical Coffin-Manson relation:

$$\frac{\Delta \varepsilon_p}{2} = \varepsilon'_f (2N)^c \quad (2.2)$$

where $\frac{\Delta \varepsilon_p}{2}$ is the plastic strain amplitude, ε'_f is the fatigue ductility coefficient, which is a constant, c is fatigue ductility exponent, which is a negative empirical constant, and N is the number of cycles to failure. With this equation, we can expect larger number of cycles before failure with smaller magnitude of plastic strain. Since nanotube structure has a smaller plastic strain accumulated after each cycle, it has a longer lifetime. This agrees with experimental results.

2.3 Analytical model for stress distribution

Both structures are axis-symmetric, it is feasible to develop an analytical model to simplify failure analysis. The model was developed by assuming linear elasticity. The finite element models were changed to compare two solutions. In this subsection, the model and comparison will be demonstrated.

Analytical solution of a tube under pressure has been developed by Timoshenko. [20] A tube with inner radius of a and out radius of b is under internal pressure of p_i and external pressure of p_o , as it is shown in Figure 2.6. The solutions of radial stress σ_r and hoop stress σ_θ are also given in the figure.

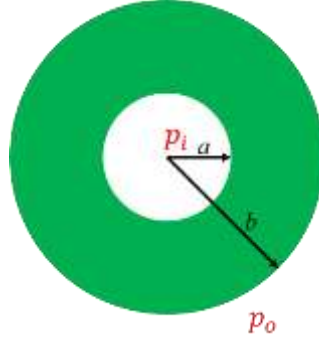


Figure 2.6: Setup of analytical solution

$$\sigma_r = \frac{a^2 b^2 (p_i - p_o)}{b^2 - a^2} \frac{1}{r^2} + \frac{p_i a^2 - p_o b^2}{b^2 - a^2} \quad (2.3)$$

$$\sigma_\theta = -\frac{a^2 b^2 (p_i - p_o)}{b^2 - a^2} \frac{1}{r^2} + \frac{p_i a^2 - p_o b^2}{b^2 - a^2} \quad (2.4)$$

Nanotube structure can be simplified as shown in Figure 2.7. With boundary conditions and continuity requirement, solution for radial stress and hoop stress were obtained by principle of superposition.

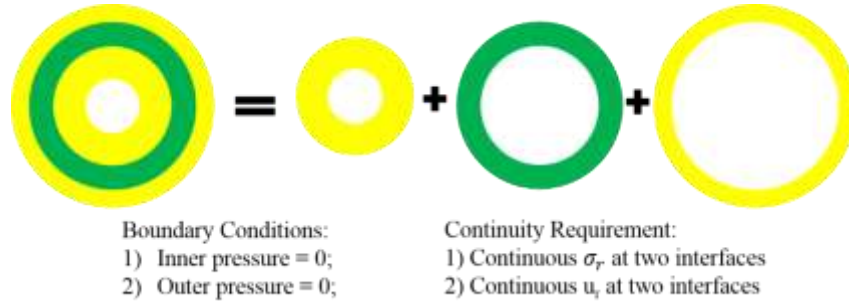


Figure 2.7: Superposition of ring structure, boundary conditions and continuity requirement

The radial stress distribution at different thickness ratio from analytical solution and numerical solution as a function of distance from the tube center is demonstrated in Figure 2.8. Even though analytical solution gave a similar distribution with numerical solutions at each thickness ratio, the large difference in magnitude shows invalidity of the analytical solution.

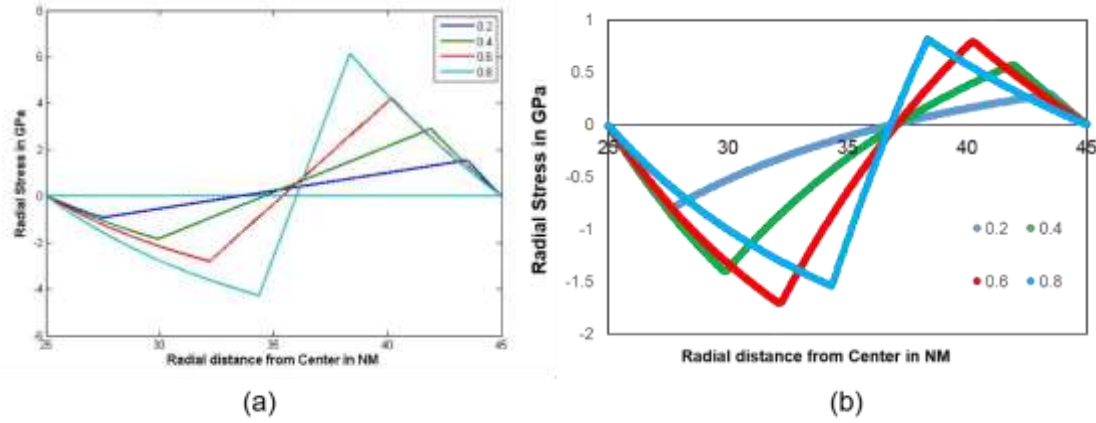


Figure 2.8: Radial stress distribution at different thickness ratio as a function of distance from the tube center: (a) from analytical solution; (b) from finite element method

In Timoshenko's solution, deformation is assumed to be small and negligible. This assumption was adopted automatically in this solution. However, the volume change of silicon after lithiation is up to 400%, which made this assumption invalid. Since we put more constrain on the structure by the assumption of small deformation, higher stress can be expected. Meanwhile, the analytical solution did take plastic deformation into consideration. It is essential to have numerical solution discussed in section 2.2.

2.4 Future work

From previous discussion, we know the failure of silicon anodes can be controlled by plastic strain. Structures that can reduce plastic strain will be beneficial. To further improve surface and volume ratio, a sinusoidal function can be used to describe inner surface of the anode, where A, B and C are three design parameters.

$$r(\theta) = A * \sin(B\theta) + C \quad (2.5)$$

Each combination of three parameters can be implemented in the finite element model, as it shown in Figure 2.9. Stress and plastic strain can be calculated correspondingly. By trading off the surface area, stress, and plastic strain, an optimal configuration can be achieved.

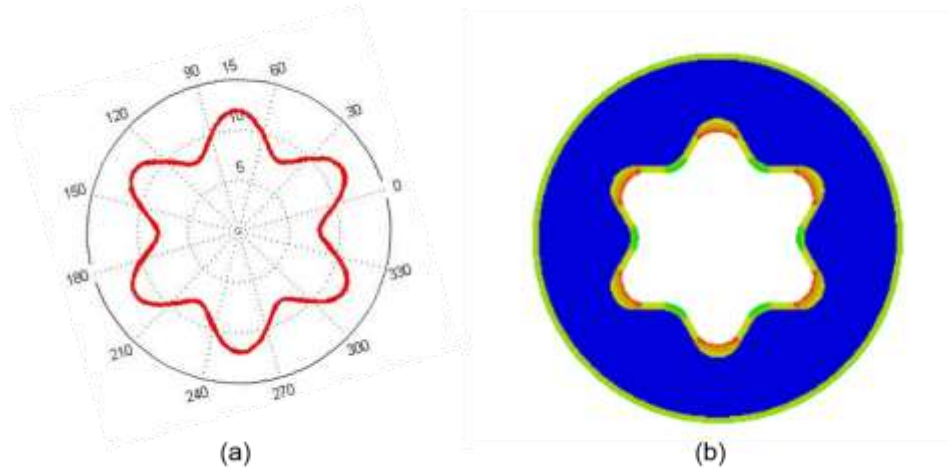


Figure 2.9: Configuration of inner surface from sinusoidal function with $A = 2$, $B=6$ and $C=10$: (a) shape of inner surface; (b) plastic strain distribution of the configuration

In the Figure 2.4 of plastic strain distribution, the plastic strain didn't remain in the lithiated silicon except that at the interface with pure silicon, because continuous lithiation process was divided into 20 steps artificially. In each step, a new model was made with different locations of material boundary updated manually. With user-defined subroutine, one can update material boundary automatically in the model. It can be more realistic. The model only studied the first lithiation cycle. The accumulation of plastic strain was not presented as a function of cycles. One can put more steps into the model and obtain the accumulation effects of plastic strain.

Chapter 3 : Modified Mohr-Coulomb Criterion

3.1 Introduction

Different failure criteria have been established to predict failure of materials. Von Mises and Tresca criteria are the most commonly applied failure criteria.[44][45][46] Both criteria use the maximum shear stress of a certain material as a critical value. If an equivalent stress calculated by different criteria overrides the maximum shear stress, failure of material is expected. The maximum shear stress of the material is assumed to be a constant in both criteria. This assumption works well for ductile materials, say, metals.[45] However, the assumption is not valid for brittle materials, such as rocks and rubbers. Maximum shear stress of rocks depends greatly on loading conditions, which causes von Mises and Tresca criteria inaccurate to predict failure. Therefore Mohr-Coulomb criterion is preferred to predict failure of brittle material, since it assumes the maximum failure stress is a function of principal stresses. [47][48][49]

Failure of rocks is an important topic in geology. To get better understanding of failure criteria, many experiments have been conducted on different types of rocks, such as Dunham Dolomite, Solenhofen Limestone, and Yunbari Shale.[50] Rock samples were compressed until failure. Loading cells kept records of compressive stress. Experimental data revealed the relationship between maximum shear stress and effective stress. It also helped to verify Mohr-Coulomb criterion.

Earthquake mechanism is closely related to failure of rocks. From previous observation, geologists find frequency of earthquakes changes along the depth of crust and mantle. Frequency has two peaks at depth of 10 – 20 km and 590 – 600km.[51][52] A new theory based on mismatch strain between crust and mantle was proposed by Song[53] to explain this phenomenon . In their model, crust and mantle had different volume reduction at different depth of the earth. Stress in crust was caused by the mismatch between crust and mantle and varied along the depth. At the same time, crust and mantle were under different compressive pressure and thus had different maximum failure stress along the depth. When the stress was greater than the maximum failure stress at the same depth, more frequent earthquakes were expected at that depth. They had built a numerical model to calculate stress in crust at different depth. A failure criterion was necessary to predict

failure stress at different depth. In this chapter, a nonlinear Mohr – Coulomb failure envelope will be demonstrated.

3.2 Failure criteria, envelopes and surfaces

If a material sample under a uniaxial loading in the direction of \vec{e}_1 , yielding of the material occurs when

$$\sigma_{11} \geq \sigma_y \quad (3.1)$$

in which σ_y is defined as yielding stress. It is the most simple failure criterion for yielding. However, multiaxial loading is more common than uniaxial loading in real problems. Thus, an equivalent stress which can represent loading condition and a critical stress beyond which yielding occurs are two essential issues of failure criteria for multiaxial loading. In this section, Tresca, von Mises and Mohr-Coulomb failure criteria will be discussed in aspect of equivalent stress calculation, critical stress definition, shape of failure envelopes and failure surfaces.

3.2.1 Tresca criterion

Tresca criterion, also called maximum shear stress criterion, states that yielding starts when the maximum shear stress in the material τ_{max} equals the maximum shear stress at yielding in a simple tension test τ_y . From Mohr's circle, maximum shear stress is calculated by

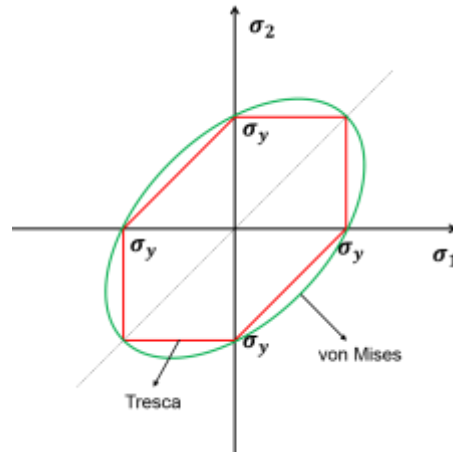
$$\tau_{max} = \frac{\sigma_{max} - \sigma_{min}}{2} \quad (3.2)$$

in which $\sigma_{max}, \sigma_{min}$ are maximum and minimum principal stress. For a plane stress loading condition ($\sigma_{33} = \sigma_{32} = \sigma_{31} = 0$), maximum shear stress can be calculated considering compressive and tensile stress as shown in Table 3.1, where σ_1 and σ_2 are principal stress.

Table 3.1: Maximum shear stress calculation

σ_1	σ_2	$2\tau_{max}$
>0	>0	σ_1 or σ_2
<0	>0	$\sigma_2 - \sigma_1$
<0	<0	$-\sigma_1$ or $-\sigma_2$
>0	<0	$\sigma_1 - \sigma_2$

A failure envelope of Tresca criterion can be drawn Figure 3.1. Inside the envelope, stresses will not yield the material. For conditions other than plane stress (σ_3 is a nonzero value), τ_{max} can be calculated with more complex methods. A failure surface can be drawn. The failure surface is shown in Figure 3.2 together with von Mises yielding surface.

**Figure 3.1: Yielding Envelope of Tresca and von Mises criteria in plane stress condition**

3.2.2 Von Mises criterion

Von Mises criterion, also called maximum distortion/shear energy criterion, states that yielding starts when the maximum distortion/shear energy in the material $W_{d,max}$ equals the maximum distortion/shear energy at yielding in a simple tension test $W_{d,y}$. Distortion energy can be expressed in term of stresses as following:

$$W_{d,max} = \frac{1}{12G} [(\sigma_{11} - \sigma_{22})^2 + (\sigma_{11} - \sigma_{33})^2 + (\sigma_{22} - \sigma_{33})^2 + 6(\sigma_{12}^2 + \sigma_{13}^2 + \sigma_{23}^2)] \quad (3.3)$$

where σ_{ij} are components in stress tensors. Distortion energy in a simple tension condition can be expressed in yielding stress.

$$W_{d,y} = \frac{1}{12G} [(\sigma_y - 0)^2 + (\sigma_y - 0)^2] = \frac{1}{6G} \sigma_y^2 \quad (3.4)$$

Therefore the general form of von Mises criterion is

$$[(\sigma_{11} - \sigma_{22})^2 + (\sigma_{11} - \sigma_{33})^2 + (\sigma_{22} - \sigma_{33})^2 + 6(\sigma_{12}^2 + \sigma_{13}^2 + \sigma_{23}^2)] = 2\sigma_y^2 \quad (3.5)$$

By coordinate transformation, stress components can be simplified with three principal stress. Distortion energy in term of principal stress is given as:

$$W_{d,max} = \frac{1}{12G} [(\sigma_1 - \sigma_2)^2 + (\sigma_1 - \sigma_3)^2 + (\sigma_2 - \sigma_3)^2] \quad (3.6)$$

For plane stress condition, when σ_3 equals to 0, the failure criterion can be further simplified as

$$\sigma_1^2 + \sigma_2^2 - \sigma_1\sigma_2 = \sigma_y^2 \quad (3.7)$$

which has an elliptical failure envelope shown in Figure 3.1. Failure surfaces of two criteria in general cases are shown in Figure 3.2. From the both figures, von Mises criterion has a greater regions compared to Tresca criterion, which means it has a looser restriction.

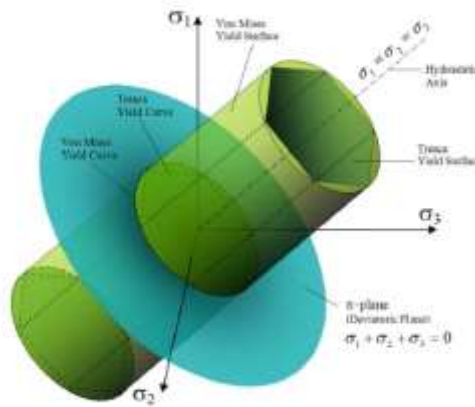


Figure 3.2: Yielding surfaces of two criteria in general cases. Adopted from "Yield surfaces" by Rswarbrick - Own work, based on Yield_surfaces.png. Licensed under CC BY-SA 3.0

3.2.3 Mohr-Coulomb criterion

Coulomb proposed the relationship between maximum shear stress τ_{max} and uniaxial compressive stress σ based on his observation on retaining walls.

$$\tau_{max} = S_0 + \sigma \tan \varphi \quad (3.8)$$

in which S_0 is the inherent shear strength and φ is the angle of internal friction. For multiaxial loading, Mohr's circles can describe different loading conditions with three principal stresses σ_I, σ_{II} and σ_{III} . Three stresses have an order that σ_I is the largest and σ_{III} is the smallest. By plotting the relationship and Mohr's circle in one plane in Figure 3.3, the relationship can be further derived with principal stresses from geometry as following

$$\frac{\sigma_I - \sigma_{III}}{2} = \left(\frac{\sigma_I + \sigma_{III}}{2} + \frac{S_0 \cos \varphi}{\sin \varphi} \right) \sin \varphi \quad (3.9)$$

$$\tau_{max} = \sigma_m \sin \varphi + S_0 \cos \varphi \quad (3.10)$$

in which σ_m is mean stress of σ_I and σ_{III} . For a certain mean stress, a corresponding maximum shear stress can be obtained from the relationship above. Fracture occurs when shear stress reaches the maximum. The yielding envelope is tangential to the Mohr's circle.

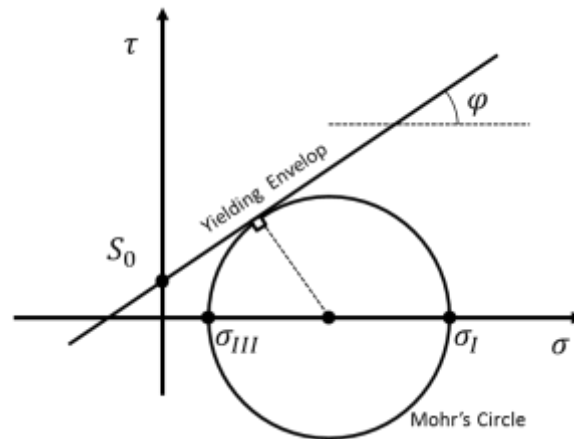


Figure 3.3: Failure Envelope of Mohr –Coulomb Criterion

For three principal stresses σ_1, σ_2 and σ_3 without order in magnitude, the failure criteria can be expressed with six equations.

$$\pm \frac{\sigma_1 - \sigma_2}{2} = \frac{\sigma_1 + \sigma_2}{2} \sin \varphi + S_0 \cos \varphi \quad (3.11)$$

$$\pm \frac{\sigma_1 - \sigma_3}{2} = \frac{\sigma_1 + \sigma_3}{2} \sin \varphi + S_0 \cos \varphi \quad (3.12)$$

$$\pm \frac{\sigma_2 - \sigma_3}{2} = \frac{\sigma_2 + \sigma_3}{2} \sin \varphi + S_0 \cos \varphi \quad (3.13)$$

Six equations give a surface shown in Figure 3.4. Since Mohr-Coulomb criterion is used to predicted failure of brittle material under compressive loading, both failure envelop and surface choose compression as positive direction of stress.

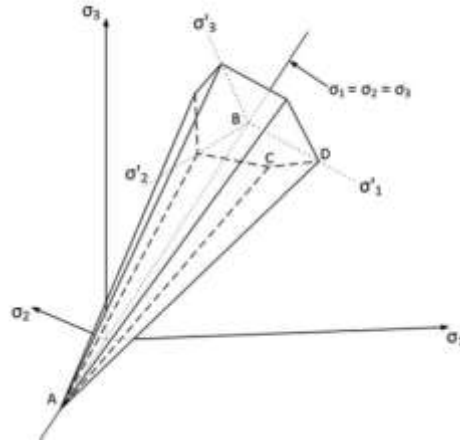


Figure 3.4: Failure surface of Mohr-Coulomb Criterion in general case[47]

From the above discussion, it requires only one material property, maximum shear stress σ_y , to determine yielding envelopes and surfaces for von Mises and Tresca criteria. Since von Mises criterion uses one universal expression for equivalent stress regardless of magnitude and directions, it is more widely used to predict failure. Mohr-Coulomb criterion requires one more parameters, angle of internal friction φ . However, it has closer approximation to experimental results from compressive tests on brittle materials, compared to other two criteria.

3.3 Experimental results from literature

Experiments were conducted on five types of rocks, Dunham dolemite, Solenhofen limestone, Shirahama sandstone, Yuubari shale, and KTB amphibolite. Three compressive stress were loaded on samples. Two smaller compressive stresses, σ_{II} and σ_{III} , were controlled. σ_I was increased to

cause failure of rocks and final σ_I was recorded. After changing controlled stresses σ_{II} and σ_{III} , experiments were repeated.

From Mohr-Coulomb criterion, a relationship between σ_I and σ_{III} can be found.

$$\sigma_I = \frac{\sigma_{III}(1 + \sin\varphi)}{1 - \sin\varphi} + \frac{2S_0\cos\varphi}{1 - \sin\varphi} \quad (3.14)$$

For the convenience of calculation, this relationship was further simplified as

$$\sigma_I = A + B\sigma_{III} \quad (3.15)$$

Both equations are independent of σ_{II} . The theoretical failure envelope and experimental data are demonstrated in Figure 3.5.

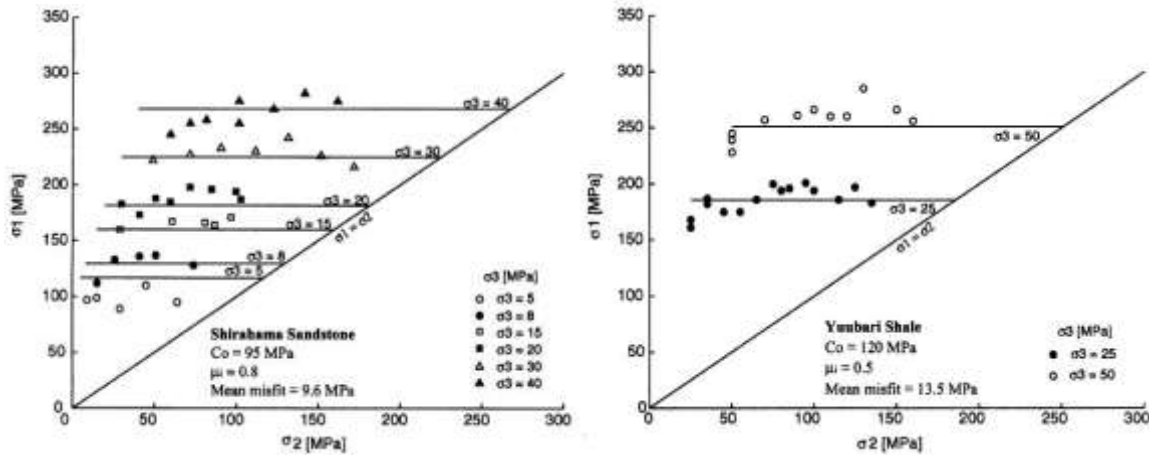


Figure 3.5: Theoretical failure envelopes and experimental results of Shirahama sandstone and Yunbari shale: straight horizontal lines are theoretical envelopes[50]

The above figures show experimental data of Shirahama sandstone and Yunbari Shale fit well with theoretical envelopes, which can verify that Mohr-Coulomb criterion gives a good failure envelope. However, experimental data also have some fluctuation with σ_{II} . This fluctuation varies a lot from different types of rocks[50]. Figure 3.6 shows experimental results of Dunham dolomite. The fluctuation with σ_{II} is too large to consider Mohr-Coulomb criterion as a good approximation. Therefore it is necessary to check if properties of rocks depend a lot on σ_{II}

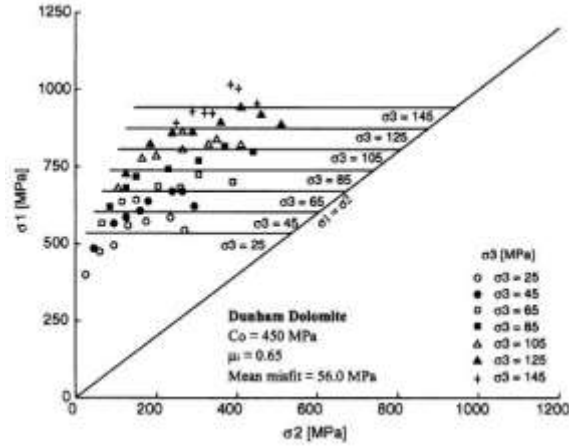


Figure 3.6: Theoretical failure envelopes and experimental results of Dunham dolemite [50]

3.4 Nonlinear Mohr-Coulomb failure envelope for earthquake frequency

From records of earthquakes in recent forty years, geologists find that earthquake frequency changes along the depth. Figure 3.7 illustrates the variation in frequency. Earthquake frequency has two peaks, one at the shallow earth around 20km and another one at the depth around 600km.

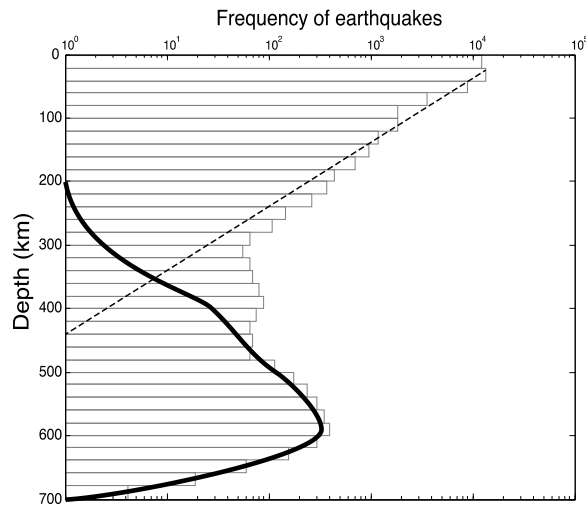


Figure 3.7: Depth distribution of global seismicity[51][52][53]

To explain this frequency distribution, Song[53] developed a subducting crust and mantle model. Crust and mantle on the shallow earth form a slab, which can be regarded as a bilayer beam. Thickness of crust is one tenth of mantle in the slab. Then crust-mantle slab subducts into the deep mantle. The model is illustrated in Figure 3.8.

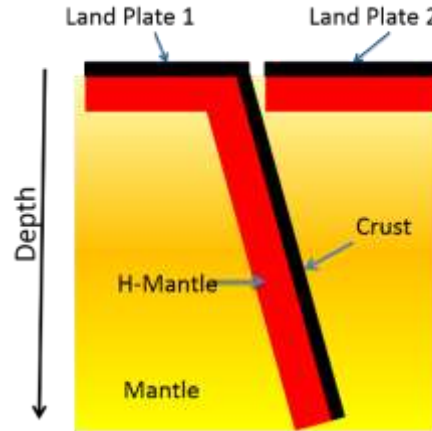


Figure 3.8: Subducting crust and mantle model

Since confining pressure increases along the depth, the slab experiences several phase changes. Phase changes lead to reduction of volume in crust-mantle slab.[53] However, volume reduction of crust and mantle at certain depth is different for their different properties. Volume reduction of crust and mantle is listed in Table 3.2. Different volume reduction between two layers results in large mismatch stress at the interface between crust and mantle. Stress varies along the depth. At the same time, crust and mantle were under different compressive pressure and thus had different maximum failure stress along the depth. When the stress was greater than the maximum failure stress at the same depth, more frequent earthquakes were expected at that depth.

Table 3.2: Volume reduction of crust and mantle at different depth [53]

Crust		Mantle	
Depth(km)	Reduction	Depth(km)	Reduction
30-100	-15%	200-410	-3%
300	-4%	410	-5%
250-450	-5%	520	-1.5%
		670	-9%

Stress at different depth could be obtained with finite element simulation. The remaining work was to find a failure envelope, beyond which earthquake happened. To get a failure envelope at different depth, the first assumption was made that confining pressure σ_{III} , inherent shear strength

S_0 and internal friction coefficient $\mu_0 = \tan \varphi$ were functions of depth h only. By this assumption, maximum failure stress can be expressed as

$$\tau_{max} = S_0(h) + \sigma_{III}(h) \tan \varphi(h) \quad (3.16)$$

Relationship between confining pressure and depth was obtained by integrating weight along the depth. From previous observation, volume change at different depth is plotted in Figure 3.9. The relationship could be approximated as two linear relationship.

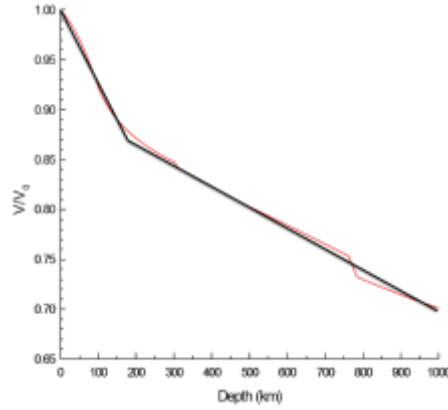


Figure 3.9: Volume change at different depth [53]

By assuming that no mass was lost during the subduction, density change could be obtained from

$$\frac{\rho}{\rho_0} = \frac{\frac{M}{V}}{\frac{M}{V_0}} = \frac{V_0}{V} \quad (3.17)$$

where M is the mass of the slab, V_0 and V are initial and final volume, ρ_0 and ρ are initial and final density. Average density at the earth surface ρ_0 is 2650 kg/m³[54]. Density at each depth could be calculated. By integrating weight along the depth, confining pressure is found. Confining pressure was plotted in Figure 3.10.

$$\sigma_{III} = \int_0^h \rho g h \, dh \quad (3.18)$$

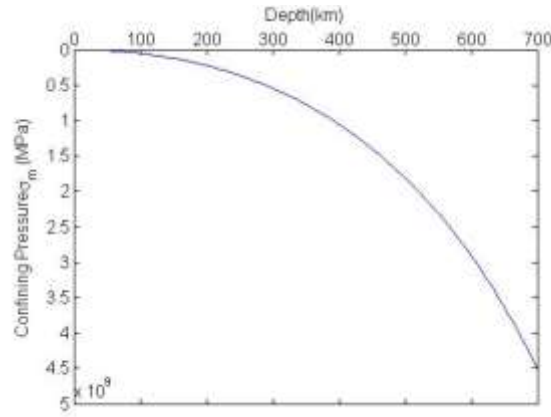


Figure 3.10: Confining pressure at different depth

Even though many experiments measuring Mohr-Coulomb parameters have been done on different types of rocks, range of confining pressure is limited and no experiments have been conducted on rocks at different depth. These situations make it difficult to find specific inherent shear stress and internal friction coefficient at different depth or confining pressure. In one previous experiment on Indian limestone, maximum compressive stress was measured at different confining pressure. Data points were fitted to different failure criteria in Figure 3.11 (a). One line can be drawn between each two adjacent points. From that line, an inherent shear strength S_0 and internal friction coefficient $\mu_0 = \tan\varphi$ can be obtained. The inherent shear strength and internal friction coefficient at different depth were obtained in the same methods and were fitted into functions as shown in Figure 3.11(b) and 3.11(c).

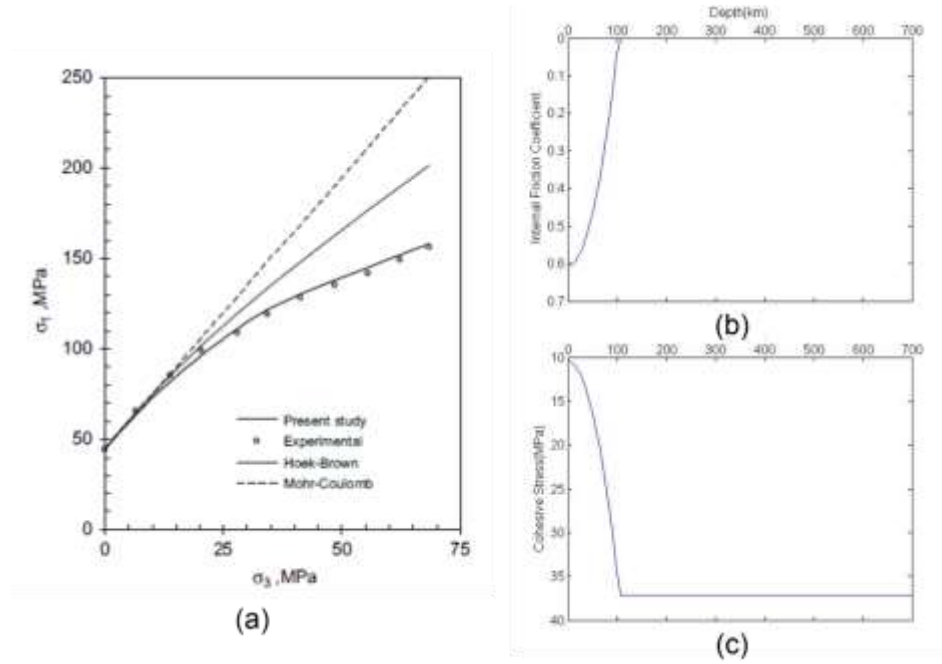


Figure 3.11: Experimental data on Indian limestone: (a) experimental data and failure criteria by other researcher; (b) internal friction coefficient as a function of depth; (c) inherent stress as a function of depth[49]

At one depth, confining pressure $\sigma_{III}(h)$ can be determined with Figure 3.10; two Mohr-Coulomb parameters, inherent stress $S_0(h)$ and internal friction coefficient $\tan \varphi(h)$, can be calculated with Figure 3.11(b) and (c). The failure envelope was obtained in Figure 3.12 by following equation,

$$\tau_{max} = S_0(h) + \sigma_{III}(h) \tan \varphi(h) \quad (3.19)$$

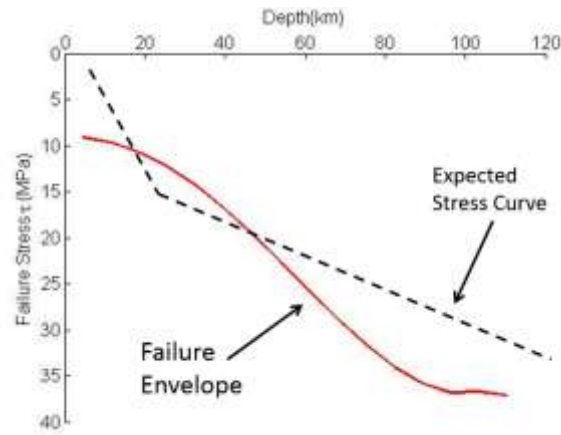


Figure 3.12: Failure envelope and expected stress curve along depth

From the figure, we can notice the non-linearity of the failure envelope. The failure stress increases gently before 20km. Then a dramatic increase happens at the range from 20km to 80km. The increase becomes gentle after 80km. The shape gives the possibility to explain the earthquake distribution along the depth. We can expect a stress curve shown in Figure 3.12. The stress increases dramatically at first and passes the failure envelope. At the depth where stress passes the envelope, the first peak of earthquake frequency can be expected. Stress increases gently and goes back within the envelope until it passes the envelope again. At that point, the second peak can be expected. In this way, two peaks in the distribution could be explained in the perspective from mechanics.

3.5 Future work

Drawback of this failure criterion came from insufficient experimental data to obtain real relationship inherent shear stress, internal friction coefficient and confining pressure, especially at the larger depth. One practical way to solve this problem is to find more experimental data on different types of rocks from literature. Two Mohr Coulomb parameters, inherent stress $S_0(h)$ and internal friction coefficient $\tan \phi(h)$, can be calculated with respect to different rocks, which is shown in Figure 3.13. If most of rocks show similar relationship, this failure criterion can be generalized to other rocks or composition of rocks. The failure criterion will be more applicable.

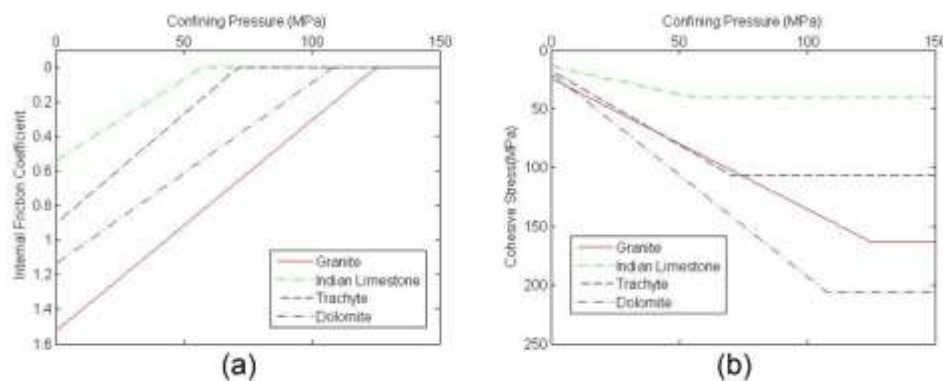


Figure 3.13: Experimental data on different rocks: (a) internal friction coefficient as a function of confining pressure; (c) inherent stress as a function of confining pressure[50]

The missing stress data and confining pressure at different depth could not verify this criterion. We would expect geologists to make more valid numerical models to calculate stress caused by different volume reduction. Or the real measurement can be done onsite.

References

- [1] F. Schreiber, "Structure and growth of self-assembling monolayers," *Prog. Surf. Sci.*, vol. 65, no. 5–8, pp. 151–257, Nov. 2000.
- [2] G. M. Whitesides and B. Grzybowski, "Self-assembly at all scales.," *Science*, vol. 295, no. 5564, pp. 2418–21, Mar. 2002.
- [3] H. Yan, S. H. Park, G. Finkelstein, J. H. Reif, and T. H. LaBean, "DNA-templated self-assembly of protein arrays and highly conductive nanowires.," *Science*, vol. 301, no. 5641, pp. 1882–4, Sep. 2003.
- [4] J. D. Hartgerink, E. Beniash, and S. I. Stupp, "Self-assembly and mineralization of peptide-amphiphile nanofibers.," *Science*, vol. 294, no. 5547, pp. 1684–8, Nov. 2001.
- [5] H. Duan and K. K. Berggren, "Directed self-assembly at the 10 nm scale by using capillary force-induced nanocoherence.," *Nano Lett.*, vol. 10, no. 9, pp. 3710–6, Sep. 2010.
- [6] D. Beebe, J. Moore, J. Bauer, Q. Yu, R. Liu, C. Devadoss, and B. Jo, "Functional hydrogel structures for autonomous flow control inside microfluidic channels," *Nature*, vol. 404, no. 6778, pp. 588–90, Apr. 2000.
- [7] M. Jamal, A. M. Zarafshar, and D. H. Gracias, "Differentially photo-crosslinked polymers enable self-assembling microfluidics.," *Nat. Commun.*, vol. 2, p. 527, Jan. 2011.
- [8] H. Li, X. Guo, R. G. Nuzzo, and K. Jimmy Hsia, "Capillary induced self-assembly of thin foils into 3D structures," *J. Mech. Phys. Solids*, vol. 58, no. 12, pp. 2033–2042, Dec. 2010.
- [9] X. Guo, H. Li, B. Y. Ahn, E. B. Duoss, K. J. Hsia, J. A. Lewis, and R. G. Nuzzo, "Two- and three-dimensional folding of thin film single-crystalline silicon for photovoltaic power applications.," *Proc. Natl. Acad. Sci. U. S. A.*, vol. 106, no. 48, pp. 20149–54, Dec. 2009.
- [10] I. S. Chun, V. B. Verma, V. C. Elarde, S. W. Kim, J. M. Zuo, J. J. Coleman, and X. Li, "InGaAs/GaAs 3D architecture formation by strain-induced self-rolling with lithographically defined rectangular stripe arrays," *J. Cryst. Growth*, vol. 310, no. 7–9, pp. 2353–2358, Apr. 2008.
- [11] I. S. Chun, A. Challa, B. Derickson, K. J. Hsia, and X. Li, "Geometry effect on the strain-induced self-rolling of semiconductor membranes.," *Nano Lett.*, vol. 10, no. 10, pp. 3927–32, Oct. 2010.
- [12] A. Azam, K. E. Laflin, M. Jamal, R. Fernandes, and D. H. Gracias, "Self-folding micropatterned polymeric containers.," *Biomed. Microdevices*, vol. 13, no. 1, pp. 51–8, Feb. 2011.
- [13] K.-U. Jeong, J.-H. Jang, D.-Y. Kim, C. Nah, J. H. Lee, M.-H. Lee, H.-J. Sun, C.-L. Wang, S. Z. D. Cheng, and E. L. Thomas, "Three-dimensional actuators transformed from the programmed two-dimensional structures via bending, twisting and folding mechanisms," *J. Mater. Chem.*, vol. 21, no. 19, p. 6824, Apr. 2011.
- [14] M. J. Motala, "Surface Patterning, Electronic Device Fabrication And, Three-Dimensional Self-Assembly Using Polydimethylsiloxane." 01-Jan-2000.
- [15] P. Yuan, "Design, fabrication, and application of stimuli-responsive hydrogel actuators." 16-Jan-2013.

- [16] D. Perltitz, “Computational design and analysis of multi-scale polymer machines.” 30-May-2014.
- [17] M. W. Hyer, “Calculation of the room-temperature shapes of unsymmetric laminates,” Mar. 1981.
- [18] M. M. Shokrieh, “Theoretical and Experimental Studies on Residual Stresses in Laminated Polymer Composites,” *J. Compos. Mater.*, vol. 39, no. 24, pp. 2213–2225, Jun. 2005.
- [19] S. Timoshenko, “Analysis of Bi-Metal Thermostats,” East Pittsburgh, PA, 1925.
- [20] S. Timoshenko and J. . Goodier, *Theory of Elasticity*, The Second. NEW YORK: McGraw-Hill Book Company, Inc, 1951.
- [21] S.-Y. MIYAZAKI, T. YASUDA, S. YOKOI, and J.-I. TORIWAKI, “An Origami Playing Simulator in the Virtual Space,” *J. Vis. Comput. Animat.*, vol. 7, no. 1, pp. 25–42, Jan. 1996.
- [22] T. C. Hull, “Origami design secrets: mathematical methods for an ancient art,” *Math. Intell.*, vol. 27, no. 2, pp. 92–95, Nov. 2008.
- [23] D. S. A. De Focatiis and S. D. Guest, “Deployable membranes designed from folding tree leaves,” *Philos. Trans. A. Math. Phys. Eng. Sci.*, vol. 360, no. 1791, pp. 227–38, Feb. 2002.
- [24] K. Miura, “Concepts of depolyable space structures,” *Int. J. Sp. Struct.*, vol. 8, no. 1, pp. 3–16, 1993.
- [25] S. A. Zirbel, R. J. Lang, M. W. Thomson, D. A. Sigel, P. E. Walkemeyer, B. P. Trease, S. P. Magleby, and L. L. Howell, “Accommodating Thickness in Origami-Based Deployable Arrays 1,” *J. Mech. Des.*, vol. 135, no. 11, p. 111005, Oct. 2013.
- [26] Z. Song, T. Ma, R. Tang, Q. Cheng, X. Wang, D. Krishnaraju, R. Panat, C. K. Chan, H. Yu, and H. Jiang, “Origami lithium-ion batteries,” *Nat. Commun.*, vol. 5, p. 3140, Jan. 2014.
- [27] K. Kuribayashi, K. Tsuchiya, Z. You, D. Tomus, M. Umemoto, T. Ito, and M. Sasaki, “Self-deployable origami stent grafts as a biomedical application of Ni-rich TiNi shape memory alloy foil,” *Mater. Sci. Eng. A*, vol. 419, no. 1–2, pp. 131–137, Mar. 2006.
- [28] S. M. Jurga, C. H. Hidrovo, J. Niemczura, H. I. Smith, and G. Barbastathis, “Nanostructured origami,” in *2003 Third IEEE Conference on Nanotechnology, 2003. IEEE-NANO 2003.*, 2003, vol. 2, pp. 220–223.
- [29] M. Piñeirua, J. Bico, and B. Roman, “Capillary origami controlled by an electric field,” *Soft Matter*, vol. 6, no. 18, p. 4491, Sep. 2010.
- [30] N. R. Geraldi, F. F. Ouali, R. H. Morris, G. McHale, and M. I. Newton, “Capillary origami and superhydrophobic membrane surfaces,” *Appl. Phys. Lett.*, vol. 102, no. 21, p. 214104, May 2013.
- [31] T. S. Shim, S.-H. Kim, C.-J. Heo, H. C. Jeon, and S.-M. Yang, “Controlled Origami Folding of Hydrogel Bilayers with Sustained Reversibility for Robust Microcarriers,” *Angew. Chemie*, vol. 124, no. 6, pp. 1449–1452, Feb. 2012.
- [32] R. Marom, S. F. Amalraj, N. Leifer, D. Jacob, and D. Aurbach, “A review of advanced

- and practical lithium battery materials,” *J. Mater. Chem.*, vol. 21, no. 27, p. 9938, Jun. 2011.
- [33] J. L. Goldman, B. R. Long, A. A. Gewirth, and R. G. Nuzzo, “Strain Anisotropies and Self-Limiting Capacities in Single-Crystalline 3D Silicon Microstructures: Models for High Energy Density Lithium-Ion Battery Anodes,” *Adv. Funct. Mater.*, vol. 21, no. 13, pp. 2412–2422, Jul. 2011.
 - [34] C. K. Chan, H. Peng, G. Liu, K. McIlwrath, X. F. Zhang, R. A. Huggins, and Y. Cui, “High-performance lithium battery anodes using silicon nanowires,” *Nat. Nanotechnol.*, vol. 3, no. 1, pp. 31–5, Jan. 2008.
 - [35] H. Wu, G. Chan, J. W. Choi, I. Ryu, Y. Yao, M. T. McDowell, S. W. Lee, A. Jackson, Y. Yang, L. Hu, and Y. Cui, “Stable cycling of double-walled silicon nanotube battery anodes through solid-electrolyte interphase control,” *Nat. Nanotechnol.*, vol. 7, no. 5, pp. 310–5, May 2012.
 - [36] H. Yang, S. Huang, X. Huang, F. Fan, W. Liang, X. H. Liu, L.-Q. Chen, J. Y. Huang, J. Li, T. Zhu, and S. Zhang, “Orientation-dependent interfacial mobility governs the anisotropic swelling in lithiated silicon nanowires,” *Nano Lett.*, vol. 12, no. 4, pp. 1953–8, Apr. 2012.
 - [37] H. Yang, F. Fan, W. Liang, X. Guo, T. Zhu, and S. Zhang, “A chemo-mechanical model of lithiation in silicon,” *J. Mech. Phys. Solids*, vol. 70, pp. 349–361, Oct. 2014.
 - [38] J. Liu, N. Li, M. D. Goodman, H. G. Zhang, E. S. Epstein, B. Huang, Z. Pan, J. Kim, J. H. Choi, X. Huang, J. Liu, K. J. Hsia, S. J. Dillon, and P. V Braun, “Mechanically and Chemically Robust Sandwich-Structured C@Si@C Nanotube Array Li-Ion Battery Anodes,” *ACS Nano*, Feb. 2015.
 - [39] X. H. Liu, J. W. Wang, S. Huang, F. Fan, X. Huang, Y. Liu, S. Krylyuk, J. Yoo, S. A. Dayeh, A. V Davydov, S. X. Mao, S. T. Picraux, S. Zhang, J. Li, T. Zhu, and J. Y. Huang, “In situ atomic-scale imaging of electrochemical lithiation in silicon,” *Nat. Nanotechnol.*, vol. 7, no. 11, pp. 749–56, Nov. 2012.
 - [40] V. A. Sethuraman, M. J. Chon, M. Shimshak, V. Srinivasan, and P. R. Guduru, “In situ measurements of stress evolution in silicon thin films during electrochemical lithiation and delithiation,” *J. Power Sources*, vol. 195, no. 15, pp. 5062–5066, Aug. 2010.
 - [41] X. H. Liu, L. Zhong, S. Huang, S. X. Mao, T. Zhu, and J. Y. Huang, “Size-dependent fracture of silicon nanoparticles during lithiation,” *ACS Nano*, vol. 6, no. 2, pp. 1522–31, Feb. 2012.
 - [42] V. A. Sethuraman, V. Srinivasan, A. F. Bower, and P. R. Guduru, “In Situ Measurements of Stress-Potential Coupling in Lithiated Silicon,” *J. Electrochem. Soc.*, vol. 157, no. 11, p. A1253, Nov. 2010.
 - [43] M. J. Chon, V. A. Sethuraman, A. McCormick, V. Srinivasan, and P. R. Guduru, “Real-Time Measurement of Stress and Damage Evolution during Initial Lithiation of Crystalline Silicon,” *Phys. Rev. Lett.*, vol. 107, no. 4, p. 045503, Jul. 2011.
 - [44] F. P. Beer, E. R. Johnston, and J. T. Dewolf, *Mechanics of Materials*, 3rd ed. New York, Toronto, London: McGraw-Hill Book Company, Inc, 2001.
 - [45] T. H. Courtney, *Mechanical Behavior of Materials*, 2nd ed. New York, Toronto, London:

- McGraw-Hill Book Company, Inc, 2005.
- [46] B. R. Lawn, *Fracture of Brittle Solids*, 2nd ed. New York: Cambridge University Press, 1993.
 - [47] J. F. Labuz and A. Zang, “Mohr–Coulomb Failure Criterion,” *Rock Mech. Rock Eng.*, vol. 45, no. 6, pp. 975–979, Jul. 2012.
 - [48] H. MATSUOKA and T. NAKAI, “Relationship among Tresca, Mises, Mohr-Coulomb and Matsuoka-Nakai failure criteria.,” *SOILS Found.*, vol. 25, no. 4, pp. 123–128, Feb. 1985.
 - [49] M. Singh, A. Raj, and B. Singh, “Modified Mohr–Coulomb criterion for non-linear triaxial and polyaxial strength of intact rocks,” *Int. J. Rock Mech. Min. Sci.*, vol. 48, no. 4, pp. 546–555, Jun. 2011.
 - [50] L. . Colmenares and M. . Zoback, “A statistical evaluation of intact rock failure criteria constrained by polyaxial test data for five different rocks,” *Int. J. Rock Mech. Min. Sci.*, vol. 39, no. 6, pp. 695–729, Sep. 2002.
 - [51] C. Frohlich, *Deep Earthquakes*. Cambridge University Press, 2006.
 - [52] E. R. Engdahl, R. van der Hilst, and R. Buland, “Global teleseismic earthquake relocation with improved travel times and procedures for depth determination,” *Bull. Seismol. Soc. Am.*, vol. 88, no. 3, pp. 722–743, Jun. 1998.
 - [53] L. Liu, J. Zhang, and X. Song, “A brittle failure mechanism for deep earthquake generation due to differential contraction forces from phase transformations,” Urbana, IL, USA, 2014.
 - [54] J. Dvorkin, *Rock Failure*. Stanford, 2001.